Alma Mater Studiorum · University of Bologna

School of Science
Department of Physics and Astronomy
Master Degree in Physics

Mechanochemistry of multi-element Mg-based complex hydrides for hydrogen storage

Supervisor:
Prof. Luca Pasquini

Co-supervisor:
Prof. Fermin Cuevas

Submitted by:
Alessia Barzotti

Academic Year 2022/2023

Contents

Abstract

The hydrogen energy chain is a crucial component of the energy transition from fossil fuels to renewable energies. Efficient and safe hydrogen storage methods are vital for its success. Reversible hydrogen storage materials with low-cost, lightweight, and versatile hydrogenation properties are needed.

This study focuses on investigating the formation of Mg_yTMH_x complex hydrides with $y = 2$ or 3 and x from 4 to 8, where TM represents $3d$ late transition metals (Fe, Co, Ni, Mn, and Cr). This will be done by combining TMs that coordinate with 2 Mg atoms to form Mg_2TMH_x (TM = Fe, Co, and Ni) and compounds with TMs that coordinate with 3 Mg atoms to form Mg_3TMH_x (TM = Mn, Cr).

Using mechanochemistry under hydrogen gas, phase formation of single-phase Mg-based complex hydrides will be analyzed. The crystal structure will be studied using X-Ray Diffraction (XRD), thermal stability will be assessed through temperature programmed desorption. Then the kinetics will be studied using the Sievert method, and PCI will also be performed.

This research aims to produce novel materials with versatile properties and gain new knowledge in the unexplored field of multi-elementary complex hydrides.

Chapter 1

Introduction

1.1 Towards a new economy based on hydrogen

The colossal and intricate machinery that has historically driven the global industrial, technological, and economic apparatus has heavily leaned on the utilization of fossil fuels, encompassing but not limited to oil, coal, and natural gas. Unfortunately, this carbon-centric economic framework, despite witnessing a profusion of remarkable technological advancements, has undeniably unleashed catastrophic repercussions on the delicate equilibrium of our environment. It has precipitated a distressing surge in the concentration of greenhouse gases within our atmosphere, constituting a significant contributor to the disquieting phenomena of global warming, climate change, and the pervasive deterioration of air quality in our urban landscapes.

The relentless and insatiable hunger for energy, contrasted with the sobering realization of the finite reservoirs of oil strewn across our planet's crust, has compelled an earnest exploration of alternative, environmentally responsible energy sources. In this landscape of contenders, hydrogen has emerged as one of the most optimistic prospects to lead the charge towards a cleaner and more sustainable energy carrier.

Hydrogen, an elemental entity, lays claim to being the most abundant substance gracing the Earth's surface. However, it carries a notable caveat: merely a fraction, a meager less than 1%, exists in its pristine molecular form (H_2), with the bulk of its presence ensnared within chemical bonds as H_2O. Notably, the chemical energy stored per unit mass of hydrogen stands at an impressive 142 mega-joules per kilogram (MJ kg^{-1}), a figure that dwarfs the energy density of conventional liquid hydrocarbons, which muster a modest 47 MJ kg^{-1} in comparison.

Furthermore, the production of hydrogen can be executed in an environmentally virtuous manner, free from carbon dioxide emissions, through the utilization of an intricate system that harnesses the capabilities of photovoltaic cells for the generation of the requisite electrical current. This electrical current, in turn, powers the electrolysis dissociation of water, culminating in the pristine production of hydrogen. Once captured and ensconced within specialized containers crafted for transportation, hydrogen stands poised for judicious utilization within fuel cells, unleashing its latent energy potential. The ensuing combustion reaction, articulated as $2H_2 + O_2 \rightarrow 2H_2O$, not only generates heat but also liberates water vapor into the atmosphere, thus marking the virtuous culmination of what is often referred to as the hydrogen cycle (Figure 1.1).[1][2]

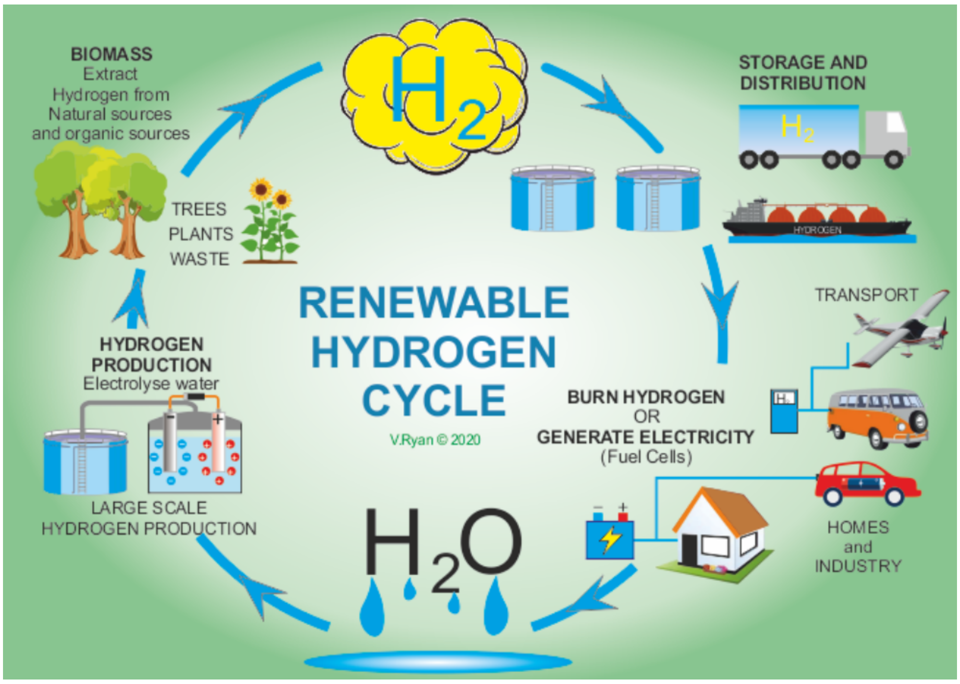

Figure 1.1: Hydrogen cycle.

In the present landscape, hydrogen represents one of the most promising alternative energy carriers on a global scale, owing to its unique attributes:

- Elevated chemical energy per unit mass.
- Diverse sources of availability.
- Eco-friendliness during utilization with near-zero CO_2 emissions.
- Potential for relatively facile distribution, considering the currently available methods of storage and transport.

However, there are two primary reasons why hydrogen has not yet assumed the role of the world's primary fuel source:

- Despite being the most abundant element in the universe, hydrogen is typically found on Earth bonded with other substances, forming water or hydrocarbons. This necessitates substantial energy input for extraction.

- Its gaseous state at ambient pressure and temperature results in a relatively large volume occupied in proportion to the energy transported, posing a challenge that common storage methods must contend with.

1.2 Hydrogen storage methods

Among the technological and scientific challenges that arise if hydrogen is to become a viable alternative to hydrocarbons, the issue of hydrogen storage is paramount. Currently, there are six different methods of hydrogen storage:

1. High-pressure gas cylinders (up to 880 bar),
2. Liquefaction in cryogenic containers (at 21 K),
3. Absorption in metallic materials, forming hydrides (under controlled conditions),
4. Adsorption of hydrogen by materials with high surface areas (at $T < 100K$),
5. Covalent or ionic compounds (at ambient pressure and temperature), and
6. Oxidation of reactive metals like Li, Na, Mg, Al, in water.

Among these methods, the most widely used are the first three, with the use of hydrides appearing to be the most promising solution, as it allows for a higher volumetric density of hydrogen compared to the other two techniques and also presents advantages in terms of safety.

One of the most significant challenges in adopting hydrogen as an alternative to fossil fuels concerns its storage and transportability. The most promising technologies currently include high-pressure gas cylinders, cryogenic liquid hydrogen tanks, and solid-state hydrogen storage using metallic hydrides.

Regarding the transport of hydrogen, it is crucial to ensure a relatively small quantity of hydrogen stored in a reasonably compact volume, always keeping user safety as a priority.

In particular, high-pressure gas cylinders and cryogenic liquid hydrogen tanks pose challenges such as high costs, considerable storage volumes, and, most importantly, the risk of hydrogen leaks, leading to safety hazards.

Solid-state hydrogen storage in metallic hydrides appears to be the most promising solution as it offers the best volumetric hydrogen storage capacity and, at the same time, is considered one of the safest options. This technology operates effectively at lower pressures, and the release of hydrogen is an endothermic process, meaning that potential vacuum seal leaks would not jeopardize user safety.

Furthermore, hydrogen released from a metallic hydride exhibits a high degree of purity and can be used directly in proton exchange membrane (PEM) fuel cells, which can achieve double or triple the efficiency of conventional gasoline engines.

To illustrate the importance of efficient hydrogen storage, consider a simple example. On average, a car can travel approximately 400 km by burning about 24 kg of gasoline.

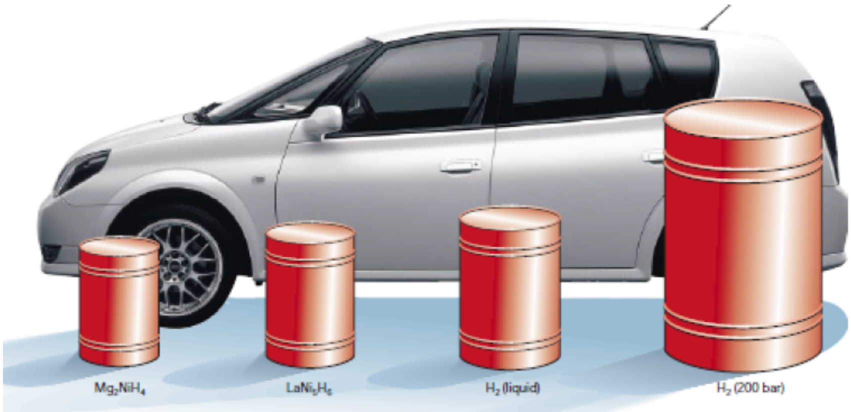

Figure 1.2: 4 kilograms of hydrogen stored using different techniques and their relative size compared to an automobile.[3]

In contrast, using a PEM fuel cell requires only about 4 kg of hydrogen, which, at room temperature and pressure, would occupy a volume of 45 m^3 (equivalent to a balloon with a 5 m diameter)[3]. This underscores the crucial need for hydrogen storage technologies that enable safe transport while reducing the volumes and weights required for storage technology.

1.3 Metal hydrides

Hydrogen, the lightest and most abundant element in the universe, is indeed the simplest element found in nature. However, on Earth, it exists predominantly in compounds rather than its pure molecular form. Pure molecular hydrogen, H_2, makes up less than 1% of the terrestrial hydrogen abundance, with the majority of hydrogen forming compounds with other elements, such as water (H_2O) or hydrocarbons (e.g. CH_4).

In some cases, hydrogen can be found within the crystalline structures of metals. This occurs when the concentration of hydrogen within these metals is significantly elevated, either as impurities or in the form of metallic hydrides. The presence of hydrogen within these materials can have significant implications, particularly in the context of hydrogen storage and materials science.

Let's delve into the thermodynamic aspects of the process governing the formation of metallic hydrides. Consider a metal M. Initially, molecular hydrogen is sparsely dispersed within the metal at very low concentrations, characterized as phase α. As the pressure of hydrogen increases, and consequently, its concentration within the metal rises, the dilution effect lessens, and a distinct hydride phase, denoted as phase β, emerges. This phase possesses its own unique lattice structure.

The chemical reaction driving this phase transformation is expressed as:

$$M + \frac{x}{2}H_2 \rightarrow MH_x + Q \tag{1.1}$$

This equation illustrates how hydrogen molecules (H_2) react with the metal (M) to form metal hydrides (MH_x), liberating energy (Q) in the process.

To understand the physical process guiding the absorption of hydrogen into the metal and the subsequent formation of a metal hydride, we can break it down into several distinct steps, which are intuitively represented in Figure 1.3.

It's crucial to note that hydrogen typically exists in a molecular form (H_2) when not in its atomic state. In the initial stages, molecular hydrogen accumulates in proximity to the metal's surface through interactions involving weak electrostatic forces like Van der Waals interactions or chemical interactions, including the formation of hydrogen bonds with surface atoms. These interactions catalyze the dissociation of hydrogen molecules into atomic hydrogen.

These atomic hydrogen atoms can then migrate into subsurface layers within the bulk metal through diffusion. This diffusion of hydrogen atoms within the bulk metal eventually enables nucleation and the formation of the hydride phase (phase β). The formation of metallic hydrides can significantly impact the properties of the metal, including its mechanical and electronic properties, making it an intriguing area of study in materials science and a potentially valuable technology for hydrogen storage, which is crucial for various energy-related applications.

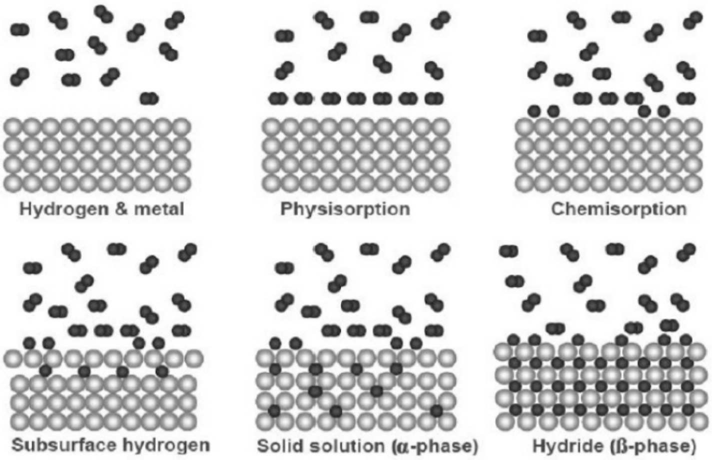

Figure 1.3: Steps of Hydrogen Absorption in a Metal[4]

1.4 Complex metal hydrides

Complex metal hydrides (CMHs), composed of light elements like boron, nitrogen, or aluminum, exhibit high hydrogen densities but suffer from inadequate thermodynamic and kinetic properties, as well as limited reversibility [5][6]. The discovery of reversibility in titanium-catalyzed $NaAlH_4$ marked a significant shift in hydrogen storage research towards complex anions[7]. Consequently, investigations expanded to include metal borohydrides such as $LiBH_4$ and nitrogen-based complex hydrides like $LiNH_2$[8]. Complex hydride anions primarily consist of covalent bonds with well-defined directionality, while ionic bonding dominates between the complex anions and counter cations (e.g., $LiBH_4$, $NaBH_4$, and $NaAlH_4$) in the solid state. Solid-state CMHs exhibit high volumetric and gravimetric hydrogen densities making them appealing for hydrogen storage applications. However, their inadequate thermodynamic and kinetic properties limit hydrogen release and uptake to elevated temperatures and pressures, rendering them unsuitable for portable applications. The hydrogen release mechanism from complex hydrides is more intricate compared to metallic and ionic hydrides, and thus not fully comprehended.

For several decades, MgH_2 has been regarded as a promising candidate for lightweight and cost-effective hydrogen storage. However, its high thermodynamic stability (with an H value of $74.1 \pm 0.4\,\mathrm{kJ \cdot mol^{-1}}$ for MgH_2) and poor kinetic properties limit the accessibility of stored hydrogen to high temperatures (e.g., $\geq 300\,^{\circ}\mathrm{C}$) and lengthy reaction times. Therefore, in order to enable widespread utilization of magnesium hydride in hydrogen storage applications, it is crucial to modify its thermodynamics and kinetics. Various approaches have been pursued for this purpose.

One of the most commonly employed methods to enhance the kinetics of Mg-based hydrogen storage materials is the use of additives. The first studies on this topic emerged in the early 1960s, and significant progress has been made from the 1970s to the 2000s Selected additives, such as Nb_2O_5, symbiotic $CeH_{2.73}/CeO_2$, ZrF_4 , $TiCl_3$ and carbon scaffolds, have demonstrated the ability to improve the kinetic properties of MgH_2. Additionally, the microstructure of MgH_2 can be modified to enhance its kinetics, for example, through high-energy ball milling. In 1961, Dymova et al. conducted ball milling of Mg powder in a hydrogen atmosphere (at 200 bar)[9]. After approximately 6 hours of milling, the formation yield of MgH_2 reached 75 %. When small amounts of additives (0.5–3 wt% I_2, CCl_4, and Mg_2Cu) were incorporated under the same conditions, the yield increased to 97 %. By continually breaking the layer of formed MgH_2 during ball milling, fresh Mg surfaces are exposed, leading to an enhanced reaction rate for MgH_2 formation MgH_2. Nowadays, ball milling is widely employed in the preparation of Mg-based hydrogen materials and is considered one of the most common methods in this field.[1]

1.5 Transition metals

The periodic table of elements represents a treasure trove of knowledge about the diversity and richness of chemistry. At its core reside the transition metals, an essential and versatile class of chemical elements, occupying a distinctive position between the alkali metals of the s-block and the elements of the p-block. This central region, known as the d-block, houses the late transition metals (iron (Fe), cobalt (Co), nickel (Ni), manganese (Mn), and chromium (Cr)) a category of particular interest for their uniqueness and numerous industrial and scientific applications.

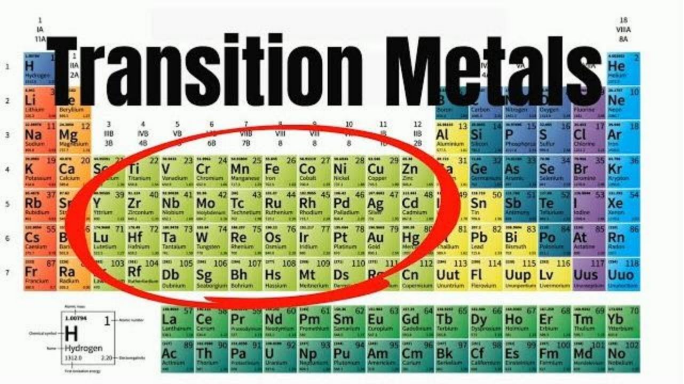

Figure 1.4: Transition metals in the periodic table

The d-block, bordering the s-block, adds an unparalleled depth to the periodic table. These metals share a similar electronic configuration, with the gradual occupation of the d orbitals, imparting them with a wide range of distinctive physical and chemical properties. Their intricate electron configurations and the presence of unpaired electrons in the d orbitals make them intriguing subjects of study for their magnetic properties.

The late transition metals, situated in groups 9 to 12 of the periodic table, are often referred to as ”extended transition metals” or ”inner transition metals” due to their unique properties and significance in both scientific and industrial contexts.

Iron, perhaps one of the most well-known and utilized elements on the entire periodic table, has long been the cornerstone of modern industry. Steel, an alloy primarily composed of iron and carbon, plays a pivotal role in construction, automotive, appliances, and numerous other applications. The importance of iron also extends to biology, as it constitutes the essential element of hemoglobin, the protein responsible for oxygen transportation in the blood.

Cobalt, with its characteristic blue-white color, is renowned for its magnetic properties. Essential in the production of permanent magnets, cobalt finds extensive use in speakers, electric motors, and electronic devices. Additionally, cobalt plays a vital role in rechargeable batteries, catalysis, and high-temperature alloys, such as cobalt steel.

Nickel, a durable and highly ductile metal, is widely employed in the production of stainless steel alloys. These alloys, with their corrosion resistance and stability at high temperatures, find application in various industrial sectors, including catalysis, batteries, electronic displays, and coinage.

Manganese, a gray-silver and brittle metal, assumes a pivotal role as an alloying element in various steel alloys, providing them with enhanced strength and hardness. Beyond its industrial applications, manganese plays a crucial role in various biological reactions, contributing to enzymatic activities and essential cellular functions.

Finally, chromium, known for its high corrosion resistance, is an essential component in the production of stainless steel, used in industries ranging from food processing to medical equipment and architectural applications.

1.6 Use complex transition metal hydrides for hydrogen storage

Over the past decade, significant progress has been made in the development of an experimental approach aimed at quantitatively analyzing in-situ hydrogen absorption within a reactive ball-milling (RBM) device. This method incorporates telemetric pressure (P) and temperature (T) sensors, enabling a comprehensive evaluation of hydrogen gas temperature during the milling process.[10] Moreover, it considers the behavior of hydrogen as a real gas. The accuracy of this method has been rigorously assessed, demonstrating a deviation within 5%, through a comparative analysis involving crystallographic and thermal desorption experiments focused on the synthesis and decomposition of magnesium (Mg) and magnesium complex hydrides with transition metals (Mg_2TM, where TM = Fe, Co, Ni).

RBM experiments conducted on mixtures of Mg and 2Mg added to TM (TM = Fe, Co, Ni) powders under a hydrogen pressure of 7.5 MPa have resulted in the formation of distinct hydride phases: MgH_2, Mg_2FeH_6[11], Mg_2CoH_5[12], and Mg_2NiH_4[13]. The reaction yield for these hydrides approximates 80%. The complete formation of hydrides is primarily constrained by the initial oxygen content within the Mg reactant. Notably, RBM under hydrogen atmosphere enables faster synthesis of Mg_2TMH_x (TM = Fe, Co, Ni) hydrides under moderate pressure and temperature conditions compared to conventional solid-gas reactions. Notably, no discernible incubation stage for hydrogen absorption is observed during the milling process.

The crystal structure of Mg_2TMH_x compounds (where TM = Fe, Co, Ni) closely resembles the high-temperature structure of the K_2PtCl_6 type. This structure belongs to the face-centered cubic (FCC) lattice system, characterized by a close-packed arrangement of atoms. In these compounds, magnesium (Mg) and the transition metal (TM) ions adopt a similar FCC arrangement to that observed in K_2PtCl_6.

In the realm of complex transition metal hydrides, the high-pressure synthesis of Mg_3CrH_8 and of Mg_3MnH_7 has garnered attention. The first compound was successfully produced under controlled conditions.[14] Through meticulous in situ examinations of 3MgH_2CrH_2 reaction mixtures at 5 GPa, the formation of the established orthorhombic phase (o-Mg_3CrH_8) was observed above 635 °C, albeit with a measured sluggishness. Remarkably, a high-temperature phase materialized rapidly at temperatures around 750°C, subsequently transforming into o-Mg_3CrH_8 upon gradual cooling. Additionally, a monoclinic polymorph, m-Mg_3CrH_8, was obtained through rapid cooling and crystallized in *P21/n* space group with distinct pentagonal bipyramidal $[CrH_7]^{5-}$ complexes and interstitial H^-, closely resembling the crystal structure of high-pressure orthorhombic Mg_3MnH_7. This resemblance indicates shared formation principles for hydrido complexes in the MgCrH and MgMnH systems, underlining the significance of these investigations for understanding hydrogen-rich materials. Calculated enthalpy-pressure relations further predict o-Mg_3CrH_8's superior stability compared to m-Mg_3CrH_8. The study underscores the power of in situ synchrotron PXRD in elucidating novel materials and encourages exploration of complex transition-metal hydrides containing elements from groups 5 and 6. Similarly, within the MgMnH system, thorough high-pressure investigations have delineated the formation conditions of two distinct complex hydrides with composition Mg_3MnH_7. The hexagonal (h-Mg_3MnH_7) and orthorhombic (o-Mg_3MnH_7) polymorphs were revealed via in situ studies, showcasing octahedral $[MnH_6]^{5-}$ complexes and interstitial H^-, with different arrangements in h- and o-Mg_3MnH_7. The orthorhombic phase transitions to monoclinic Mg_3MnH_7 upon decompression, underscoring the role of pressure in phase transformations. The electronic structures of polymorphs reflect the 18-electron complex $[MnH_6]^{5-}$ complexes and interstitial $H^-$and the significance of in situ studies in revealing complex transition metal hydride behaviors.[15] The 18-electron rule is a guideline used in organometallic chemistry to predict the stability and reactivity of transition metal complexes, particularly those involving transition metals in the d-block of the periodic table. The rule states that transition metal complexes tend to be more stable and less reactive when they have a total of 18 valence electrons around the metal center. These valence electrons can come from a combination of metal d-electrons, ligand electrons, and any additional electrons from negative charges or anionic ligands. The goal is to reach a total of 18 valence electrons. When a complex follows this rule, it tends to be more stable and less likely to undergo reactions that would alter its electron count significantly. Transition metal complexes that deviate significantly from the 18-electron rule may be more reactive and prone to undergoing chemical reactions to achieve the stable 18-electron configuration. Investigation of the in-situ hydrogen uptake curve during the synthesis of Mg_2TM complex hydrides reveals a two-step hydrogen absorption process for TM = Fe and Co, while a single absorption step is observed for the Ni case. However, complementary X-ray diffraction (XRD) analysis conclusively demonstrates that the synthesis of Mg_2TM complex hydrides occurs through a singular reaction pathway, involving a two-step process with the formation of MgH_2 as an intermediate phase. The formation kinetics of this intermediate phase is enhanced by the presence of transition metals (TM). Remarkably, faster kinetics are also observed during the decomposition of Mg_2TM hydrides compared to MgH_2, a phenomenon attributed to the influence of TM phases in the system.

Inspired by the rich chemistry of high entropy alloys, phase formation for multiple combination of these metals to form single-phase Mg-based complex hydrides will be analyzed using mechanochemistry under hydrogen gas. For this project the propose is to study the formation of Mg-based Mg_2TMHx complex hydrides with TM = 3d late transition metals such as Fe, Co, Ni, Mn and Cr. The crystal structure of as-milled compounds will be studied by X-Ray Diffraction (XRD) and their thermal stability analyzed by temperature programmed desorption.

The study of Mg_2FeH_6, was guided by its unique and characteristic in hydrogen capacity and thermodinamics. Ternary hydrides containing magnesium often exhibit high hydrogen storage capacities, which are essential for hydrogen storage applications. Mg_2FeH_6 is known to have a relatively high hydrogen storage capacity of 6 H/u.f., making it an intriguing candidate for hydrogen storage systems. The quaternary $Mg_2Fe_{0.5}Co_{0.5}H_x$compound was chosen to tailor the material properties by incorporating different transition metals [3]. The combination of iron (Fe) and cobalt (Co) in this compound offers a potential advantage. For instance, Fe-based hydrides often have good hydrogen absorption kinetics, while Co-based hydrides may contribute to further improvements in thermodynamics and stability [3]. The combination of both metals could lead to a balanced material with overall enhanced performance. The decision to investigate the unknown multi-substituted compound $Mg_y(Fe, Co, Ni, Mn, Cr)H_x$ with y = 2 and 3 was driven by the objective of exploring a wider range of compositions to optimize the material properties. The introduction of multiple elements, such as Fe, Co, Ni, Mn, and Cr, into the alloy, was aimed to customize its characteristics, including hydrogen absorption kinetics, thermodynamics, and reversibility. This approach allows for a systematic exploration of how different combinations of elements affect the hydride's formation and performance, providing a diverse array of materials to consider for specific applications. The choice of y = 2 and 3 indicates different magnesium contents in the alloy. This decision was motivated by the desire to investigate the influence of magnesium concentration on formation stability studying the two families of Fe, Co and Ni with coordination with 2 Mg atoms and Mn and Cr with coordination with 3 Mg atoms. Moreover, a higher magnesium content can significantly impact hydrogen storage capacities and kinetics. Indeed, the hydrides previously studied formed by magnesium and manganese and magnesium and chromium were Mg_3MnH_7 and Mg_3CrH_8. By studying alloys with different magnesium contents, the effects of compositional changes on the overall performance of the hydride can be analyzed.

1.7 The Van't Hoff equation

The formation of hydrides can be elucidated by the equation:

$$M + x\frac{1}{2}H_2 \to MH_x + \Delta H \tag{1.2}$$

This double arrow signifies a dynamic equilibrium between reactants and products, allowing for the reversible conversion between them by simply altering the reaction conditions. The presence of energy on the right-hand side of the equation underscores the exothermicity of absorption, namely the release of energy during the hydrogenation of the metal, concomitant with the endothermicity of the reverse process. As the reaction occurs at constant pressure, the energy also represents the enthalpy (or heat of formation) of the reaction. It is common practice to consider the enthalpy of formation as an indicator of the stability of a compound, in this case, the hydride. The higher its value, the stronger the bond between the metal and hydrogen.

In analytical terms, the energy balance is governed by the Van't Hoff equation:

$$\ln\left(\frac{P_{eq}}{P_0}\right) = \frac{-\Delta H}{RT} + \frac{\Delta S}{R} \tag{1.3}$$

Here, P_{eq} denotes the plateau pressure, P_0 is the atmospheric pressure, ΔH and ΔS represent the changes in enthalpy and entropy during the transition from metal plus hydrogen to hydride, T is the reaction temperature, and R is the gas constant (8.314 $\mathrm{J/K \cdot mol}$). The logarithmic dependence of the plateau pressure (ln) on the reciprocal of temperature is evident. The term ΔS primarily arises from the dissociation of hydrogen molecules into atomic hydrogen, while ΔH characterizes the stability of the metal-hydrogen bond in the hydride phase, varying with the specific metal considered and ascertainable from the slope of the line.

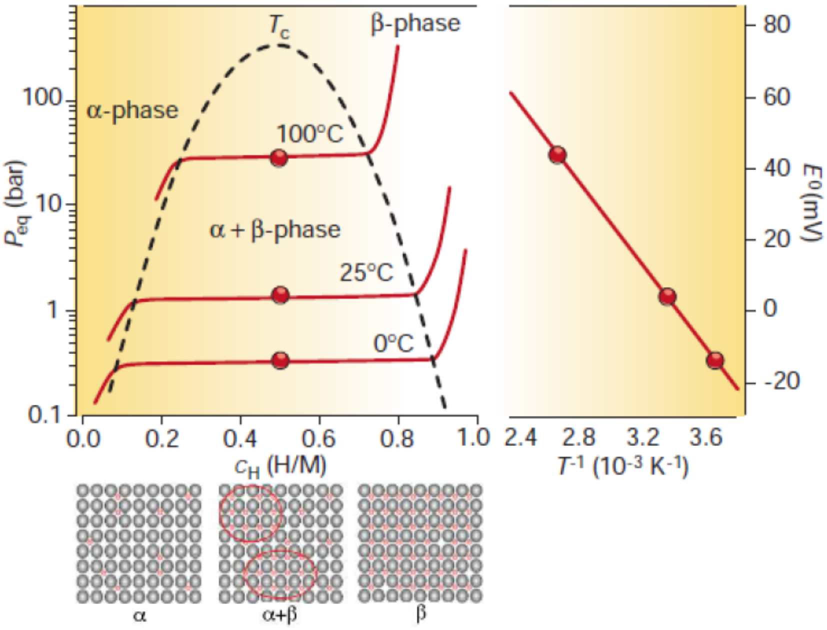

Figure 1.5: PCI plot and Van't Hoff plot for $LaNi_5$

Chapter 2

Materials and Methods

2.1 Ball milling

Ball-milling is a cost-effective and environmentally friendly technology that utilizes mechanical actions such as shear, friction, collision, and impact to modify and decrease the size of starch particles to the nanoscale. This technique belongs to a group of physical modification methods employed to reduce the relative crystallinity of starch and enhance its digestibility for improved functionality. Through ball-milling, the surface morphology of starch granules is altered, leading to an increase in overall surface area and texture. This process can also enhance functional properties such as swelling, solubility, and water solubility when supplied with increased energy. Additionally, the increased surface area of starch particles and the subsequent rise in active sites facilitate chemical reactions and induce changes in structural transformations, as well as physical and chemical properties.

Ball milling involves subjecting solids to continuous stress, aggregation, and agglomeration, enabling material interactions and chemical reactions under mechanical forces. In a high-energy mill, a hollow cylindrical container holds the material to be milled, along with balls made of stainless steel, ceramic, or rubber. The container rotates in one direction, causing the balls to rotate in the opposite direction, resulting in alternating centrifugal forces. Frictional forces act on the material as the balls roll on the inner side of the grinding jar. When the balls strike the opposite wall of the container, they impart a powerful impact force. This ball motion provides the material with sufficient kinetic energy to break chemical bonds and reduce particle size. The process involves successive mass and energy transfer, and the mechanical stress disrupts the lattice structure of the material. Optimizing ball mill parameters such as speed, grinding time, ball-to-powder ratio, milling load, milling energy, and the use of humectants is crucial to achieve desired size reduction without particle damage. Friction between starch granules during ball milling generates heat, resulting in property modifications.

Ball milling of solid particles through mechanical force combines impact, shear, and friction forces (Figure 2.1).

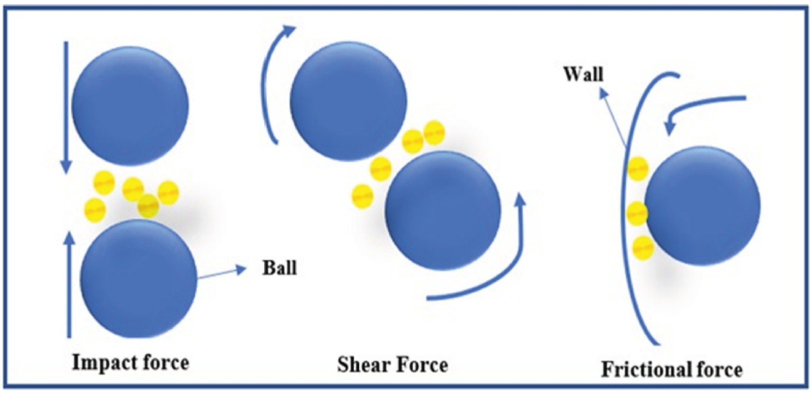

Figure 2.1: Mechanism of ball-milling

Initially, the impact force from the balls compresses the particles, flattening them. This is followed by an intermediate stage where the mixture breaks down into micrometer-scale fragments, yet still lacks homogeneity. In the final stage, further comminution occurs, leading to a physically homogeneous mass at the microscopic level. The completion stage indicates that no further physical improvement in dispersion is possible. At this point, the particles become highly deformed with metastable structures, and lamellae are no longer observable under optical microscopy. The mechanical agitation caused by the balls fragments the macro starch granules, resulting in a decrease in average particle size. Particle fragmentation and size reduction primarily depend on the starch source, composition, and amylopectin branching.

Planetary ball mill is a type of milling technique (Figure 2.2).

Figure 2.2: Platenary ball-milling

Planetary ball mills are known for their simplicity and efficiency in producing finely ground or pulverized materials. Typically, the mill consists of two or more jars mounted on a sun wheel, which rotates at a specific angular velocity while the jars rotate at their axis with another specific angular velocity. The jars are typically made of Teflon or stainless steel and are tightly sealed. In this configuration, the grinding jar and the sun wheel rotate in opposite directions, causing the milling balls to experience combined rotational motion. The interplay of two centrifugal fields within the chamber creates a non-uniform acceleration. The kinetic energy of the milling balls, generated by the Coriolis and centrifugal forces, is approximately 100 times greater than the gravitational force. The milling speed, grinding time, and ball-to-powder ratio have an impact on the resulting particle size and morphology of the solid particles.

2.2 Reactive ball milling

Reactive ball milling is a method of chemical synthesis that utilizes the combination of reactive powders and mechanical fracturing energy provided by grinding balls in a dedicated milling jar. During the process, grinding balls are rotated at high speed inside the jar, generating impact forces that crush the reactive powders and promote high-energy chemical reactions. In a specific reactive ball milling experiment, a stainless-steel jar with volume of 173 cm^3 was used, which featured pressure and temperature transducers as well as an antenna for transmitting these signals. This feature allowed for monitoring and controlling the reaction conditions during the reactive milling process. Inside the jar, 41 stainless-steel balls with a diameter of 12 mm were placed, weighing approximately 280 g in total. The reactive powders in Table 2.1 were introduced to produce 3 grams of final material. However, due to losses during jar cleaning and scraping, typically between 2 and 2.5 grams of final material are obtained. The Pulverisette P6 machine manufactured by Fritsch was used to perform the reactive ball milling experiment (Figure 2.3). The syntheses were carried out by alternating 100 cycles of 3 minutes of ball milling with 9 minutes of rest.

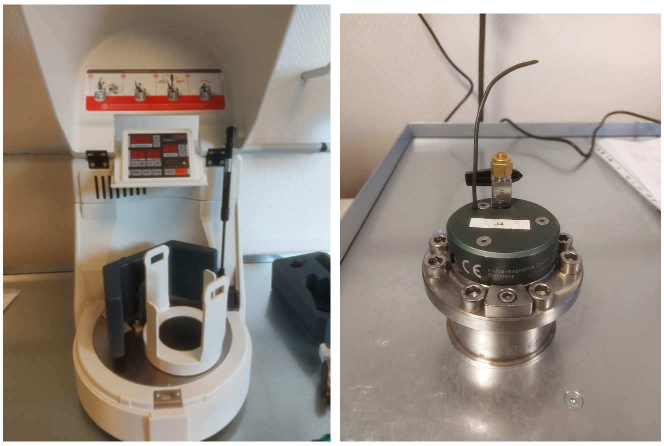

Figure 2.3: Reactive ball-milling

2.2.1 Calibrated volume

To calibrate the volume of the vial, it is necessary to use a hydrogen bank.

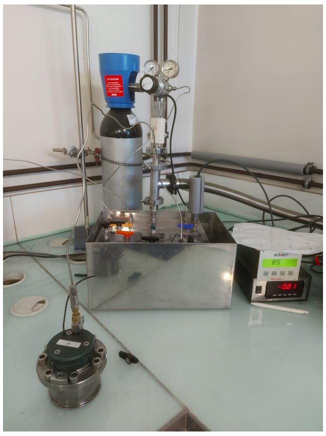

Figure 2.4: Calibration of the vial

After vacuum-sealing the connections, reservoir, bank, and vial, the calibration process can begin. With the valve of the vial closed, 70 bar of hydrogen is introduced into the combined volume of the bank, reservoir, and connection. The precise pressure volume is recorded. Subsequently, the connection valve with the vial is opened, allowing the hydrogen to flow into the vial and expand until reaching equilibrium pressure. By knowing the initial and final pressures, the volume can be evaluated using the Hemmes approximation method.

Sample	Targeted sample composition	Initial metal reactants	Element	Purity (%)	Particle size (μm)	Mass (g)
A	Mg_2FeH_6	$2\,Mg + Fe$	Mg (Alfa Aesar)	99.8	$150 < Ps < 850$	1.3965
		$2\,Mg + 0.5\,Fe + 0.5\,Co$	Fe (Chempur)	99.9	$74 < Ps < 149$	1.6006
B	$Mg_2Fe_{0.5}Co_{0.5}H_x$	$2\,Mg + 0.3\,Fe + 0.3\,Co + 0.3\,Ni$	Mg (Alfa Aesar)	99.8	$150 < Ps < 850$	1.3760
		$2\,Mg + 0.25\,Fe + 0.25\,Co + 0.25\,Ni + 0.25\,Mn$	Fe (Chempur)	99.9	$74 < Ps < 149$	0.7902
		$3\,Mg + 0.25\,Fe + 0.25\,Co + 0.25\,Ni + 0.25\,Mn$	Co (Cerac)	99.8	$Ps < 44$	0.8338
C	$Mg_2Fe_{0.3}Co_{0.3}Ni_{0.3}H_x$	$2\,Mg$ + C.alloy	Mg (Alfa Aesar)	99.8	$150 < Ps < 850$	1.3777
		$3\,Mg$ + C.alloy	Fe (Chempur)	99.9	$74 < Ps < 149$	0.5272
			Co (Cerac)	99.8	$Ps < 44$	0.5598
			Ni (Cerac)	99.9	$Ps < 44$	0.5496
D	$Mg_2Fe_{0.25}Co_{0.25}Ni_{0.25}Mn_{0.25}H_x$		Mg (Alfa Aesar)	99.8	$74 < Ps < 149$	1.3766
			Fe (Chempur)	99.9	$74 < Ps < 149$	0.3953
			Co (Cerac)	99.8	$Ps < 44$	0.4154
			Ni (Cerac)	99.9	$Ps < 44$	0.4182
			Mn (Cerac)	99.6	$Ps < 44$	0.3861
E	$Mg_3Fe_{0.25}Co_{0.25}Ni_{0.25}Mn_{0.25}H_x$		Mg (Alfa Aesar)	99.8	$150 < Ps < 850$	1.6826
			Fe (Chempur)	99.9	$74 < Ps < 149$	0.3221
			Co (Cerac)	99.8	$Ps < 44$	0.3399
			Ni (Cerac)	99.9	$Ps < 44$	0.3386
			Mn (Cerac)	99.6	$Ps < 44$	0.3168
F	$Mg_2Fe_{0.2}Co_{0.2}Ni_{0.2}Mn_{0.2}Cr_{0.2}H_x$		Mg (Alfa Aesar)	99.8	$150 < Ps < 850$	1.3917
			CA. (ICMPE Particle size)	35		1.6029
G	$Mg_3Fe_{0.2}Co_{0.2}Ni_{0.2}Mn_{0.2}Cr_{0.2}H_x$		Mg (Alfa Aesar)	99.8	$150 < Ps < 850$	1.6953
			CA. (ICMPE Particle size)	35		1.3087

Table 2.1: Nominal composition of targeted hydrides and used reactants

2.2.2 Hemmes' Approximation

Hemmes' approximation constitutes a simplified method employed within the realm of thermodynamics for the computation of real gas volumes, predicated upon the van der Waals equation of state. This approximation relies on the assumption of pressure-dependent parameters governing excluded volume and intermolecular interactions, while maintaining their independence from temperature variations. To comprehensively understand this approximation, let us dissect its fundamental principles and procedural steps.

The van der Waals equation of state serves as the foundational framework for describing the behavior of real gases, endeavoring to ameliorate the ideal gas law's limitations. It accounts for two critical factors: the finite size of gas molecules and the attractive forces prevailing among them. The equation is elegantly articulated as:

$$\left(P + \frac{an^2}{V^2}\right)(V - nb) = nRT \tag{2.1}$$

Herein:

- P signifies the gas pressure.
- V denotes the volume of the gas.
- n conveys the number of moles of the gas.
- T embodies the absolute temperature.
- R assumes the role of the gas constant.
- a and b represent the van der Waals parameters.

Hemmes' approximation streamlines the van der Waals equation by making the presumption that the attractive parameter a is contingent upon pressure alterations but remains impervious to temperature variations. This implies that a may fluctuate with changes in pressure while sustaining constancy across diverse temperatures. Furthermore, the excluded volume parameter b is similarly conjectured to be pressure-dependent but indifferent to temperature fluctuations.

In circumstances characterized by elevated pressures, the thermal contribution to the equation of state assumes a marginal role, with the gas's conduct predominantly shaped by the interplay of attractive forces and excluded volume. In this high-pressure domain, the equation of state finds an approximation rooted in the 0 K isotherm. This entails treating the gas as if it were existing at absolute zero temperature.

The accuracy of the equation of state at high pressures hinges upon the trustworthiness of the 0 K isotherm employed. This facet occupies paramount importance within the context of Hemmes' approximation, as it effectively replaces temperature-dependent terms with their counterparts evaluated at absolute zero.

Hemmes' approximation makes the postulation that the influence exerted by the melting line, delineating the phase transition from solid to liquid, upon the equation of state within the fluid phase remains inconsequential and can be disregarded. This streamlined modeling approach circumvents the necessity of formulating a novel equation of state specific to the fluid phase.

2.3 X-ray diffraction

X-ray diffraction is a widely used technique in materials science and crystallography to analyze the composition, crystalline structure, and properties of various materials. It provides valuable insights into the arrangement of atoms within a sample, helping researchers understand its properties and behavior.

In X-ray diffraction, a monochromatic beam of X-rays is directed towards the sample. The choice of X-rays is crucial because their wavelength is similar to the spacing between atoms in the crystal lattice. This similarity enables the X-rays to interact with the atoms and produce a diffraction pattern.

When the X-rays interact with the atoms in the crystal lattice, they are scattered in different directions. This scattering occurs due to the interference of the X-rays with the electron clouds surrounding the atoms. The scattered X-rays form a diffraction pattern, which is captured on a detector.

The diffraction pattern consists of a series of spots or peaks that correspond to the constructive interference of the scattered X-rays. Each peak in the pattern represents a specific set of atomic planes within the crystal lattice. By analyzing the positions and intensities of these peaks, researchers can determine the crystal structure, including the arrangement of atoms, the distances between them, and the angles between different crystal planes.

Bragg's law is used to relate the angle of diffraction, the wavelength of the X-rays and the spacing between atomic planes:

$$2d\sin(\theta) = n\lambda \tag{2.2}$$

Where 'd' is the distance between adjacent atomic planes, 'θ' is the angle of diffraction, 'n' is an integer representing the order of the diffraction peak, and 'λ' is the wavelength of the X-rays. By measuring the diffraction angles and knowing the X-ray wavelength, researchers can calculate the interplanar spacing and thus obtain valuable information about the crystal structure.

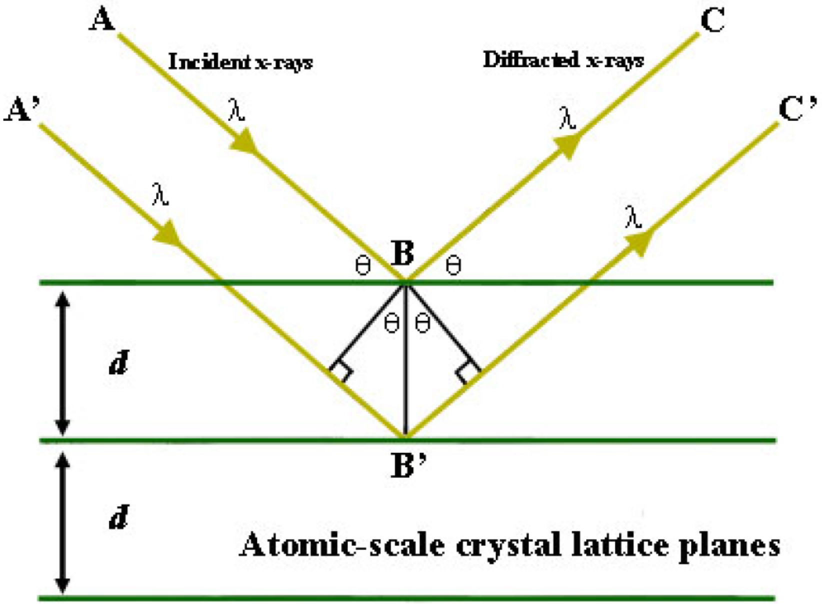

Figure 2.5: Bragg's Law reflection. The diffracted X-rays exhibit constructive interference when the distance between paths ABC and A'B'C' differs by an integer number of wavelengths (λ).

X-ray diffraction is not limited to large crystals. It can also be applied to nanocrystalline materials, powders, and even amorphous substances. In such cases, the diffraction pattern provides information about the average crystal size, degree of crystallinity, and the presence of any preferred orientations in the sample.

X-ray diffraction is a versatile technique that provides valuable insights into a sample's composition and crystalline structure. By measuring the intensity of signals at different angles of diffraction (represented as two theta positions), X-ray diffraction plots offer crucial information about the arrangement of crystals or atoms within the sample.

Figure 2.6: Experimental apparatus

The intensity of the peaks in the plot directly correlates to the abundance of molecules in specific phases or with distinct atomic spacings. A higher peak intensity signifies a greater quantity of crystals or molecules with that particular spacing. This intensity measurement enables quantitative analysis and the determination of phase purity.

Furthermore, the width of the peaks provides insights into the sample's crystal size. Narrower peaks indicate larger crystals, while broader peaks suggest smaller crystals, defects in the crystalline structure, or the presence of amorphous regions where perfect crystallinity is absent.

X-ray diffraction patterns serve as unique fingerprints for different elements, compounds, and minerals. By comparing the diffraction pattern of an unknown sample to established databases, one can identify and verify the composition of the sample. The locations, widths, and relative intensities of the diffraction peaks are compared with known patterns to establish a match and confirm the presence of specific elements or compounds. In this case, a cobalt X-ray source with two wavelengths $\lambda_{\alpha 1} = 1.788965$ Å and $\lambda_{\alpha 2} = 21.792850\AA$ and relative ratio of 50% was used.

2.3.1 Preparation of oxygen and moisture sensitive samples

The preparation of air-reactive samples for X-ray diffraction analysis involves working in a controlled environment devoid of oxygen and moisture. To achieve this, an argon-filled glovebox is used to create an inert and protective atmosphere. Inside the glovebox, strict precautions are followed to prevent contamination and exposure to air.

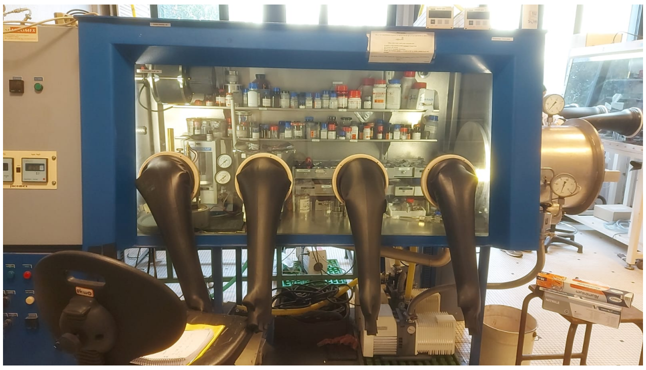

Figure 2.7: Argon filled glovebox

The process begins with carefully selecting and weighing the materials needed for sample formation. It is crucial to ensure the materials are pure and free from moisture. Next, the materials are homogeneously mixed or deposited onto an appropriate substrate for X-ray diffraction analysis. Throughout the process, specialized tools and containers suitable for the inert environment are used to prevent any contamination.

Once the sample is prepared inside the glovebox, it needs to be securely sealed to prevent exposure to external air. This can be done using glass capsules or specific supports designed for X-ray diffraction that can be hermetically sealed. After sealing the sample, it can be safely transferred out of the glovebox while maintaining the integrity of the inert atmosphere. Careful attention is given to avoid any external contamination during the transfer.

Figure 2.8: Sample under glass capsule

With the sample prepared, X-ray diffraction analysis can be performed using the appropriate equipment. X-ray diffraction provides detailed information about the sample's crystalline structure, composition, and other relevant properties.

It is important to highlight that the preparation of air-reactive samples inside an argon glovebox requires specific skills and meticulous attention to ensure sample integrity and the accuracy of X-ray diffraction analysis results.

2.4 Temperature Programmed Desorption

Temperature-programmed desorption (TPD) is a technique used to monitor surface events occurring on solid substances while changing the sample's temperature with a programmed heating rate ($\beta(t) = \frac{dT}{dt}$). TPD can be used to investigate various surface processes, including desorption, reduction, oxidation, and sulfidation, which are monitored using temperature-programmed reduction (TPR), temperature-programmed oxidation (TPO), and temperature-programmed sulfidation (TPS), respectively. TPD is applicable for studying both porous materials (such as catalysts) and well-defined surfaces of single-crystalline samples. It is a simple and cost-effective technique, which explains its widespread use in scientific research. TPD originated from flash desorption, a method developed in the 1950s to investigate the kinetics of molecular desorption from single crystal surfaces under high vacuum conditions. Flash desorption involved adsorbing a known gas on a clean sample and then heating it to induce desorption. The resulting pressure-time curve, known as a ”desorption spectrum,” provided information about the desorption process. Flash desorption was primarily used for studying low-surface area substances, but it was later adapted for high-surface area materials under ambient pressure conditions.

Amnenomiya and Cvetanović further developed flash desorption for catalytic studies. Their modified technique, known as ”temperature-programmed desorption,” allowed controlled heating of the sample and simultaneous study of chemisorption and surface reactions. They discovered the existence of different active sites for the adsorption of ethylene on alumina and determined the energy values for ethylene desorption. Since then, TPD has been extensively developed, with improvements in experimental setups and applications for various types of reactions.

There are two main types of TPD equipment: ultrahigh vacuum systems used for investigating single-crystalline samples and ”flow” systems used for porous materials. TPD provides valuable information about the rate of desorption of adsorbed molecules as a function of temperature, allowing the identification and characterization of active sites in adsorption and catalytic reactions. It helps in understanding adsorption states, binding energies, surface concentrations, and desorption kinetics. TPD is widely used for catalyst characterization, particularly in studying kinetic and thermodynamic parameters of absorptio/desorption and decomposition processes.

The experimental setup used consists of a component composed of various volumes, tubes, junctions, and valves (both manual and pneumatic), as well as temperature and pressure sensors, and a data recording system. The system is depicted in the figure 2.9.

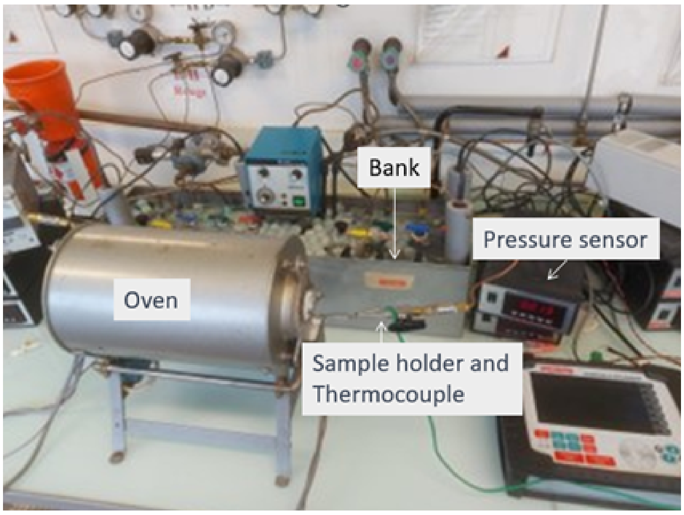

Figure 2.9: Experimental apparatus

TPD experiments were performed from 30 to 375 °C degrees at a heating rate of 2 K/min, generally using between 250 and 300 mg of each sample in a volume of 128.7 cm^3. As the temperature increases, the hydrogen atoms were desorbed to form hydrogen gas in molecular form. The pressure increase is proportional to the release of hydrogen atoms.

2.5 Absorption and desorption kinetics by solid-gas reaction, Sieverts' method

It's worth mentioning that the Sievert method provides a reliable means to measure hydrogen absorption in materials, particularly metals, and plays a crucial role in various industries such as hydrogen storage, fuel cells, and hydrogen embrittlement studies. The method allows for quantitative analysis of hydrogen concentrations and its impact on material properties. The primary measurement of utmost importance for evaluating a novel hydrogen storage material is the pressure-composition isotherm. This fundamental analysis captures critical data regarding the storage conditions and the quantity of hydrogen stored within the material. The prevailing experimental technique employed to construct such isotherms is the Sieverts technique. In this method, the amount of hydrogen absorbed or desorbed by the sample is inferred through precise measurements of the hydrogen pressure during a stepwise procedure. This approach allows for a comprehensive examination of the various factors that contribute to optimal performance, based on a model that considers the sensitivity of the Sieverts manifold to variations in hydrogen uptake.

In such measurements, important typical aspects of this measurement can be gleaned: the driving force of the process is the degree of perturbation applied to the system; the greater the pressure change, the higher the rate at which the sample absorbs or desorbs. The rate of change in the concentration of hydrogen in the metal is generally higher in the initial stages, just after the perturbation is applied, while it decreases more and more as it approaches equilibrium

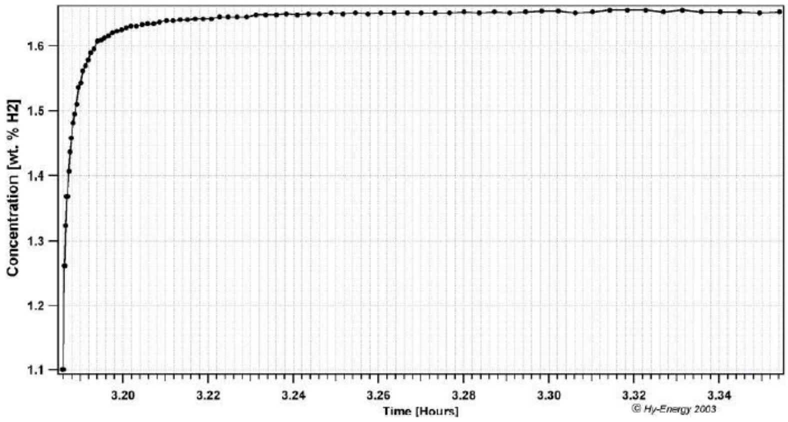

Figure 2.10: Typical absorption kinetics, where you can observe the characteristic concentration profile over time until reaching equilibrium

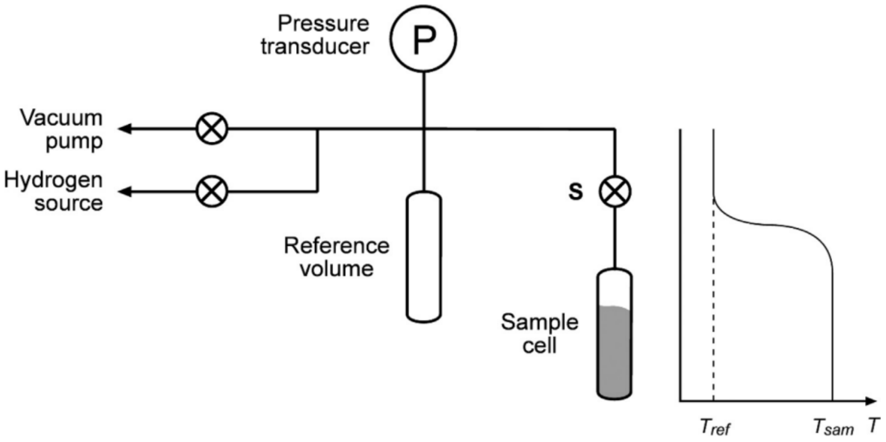

Figure 2.11: Typical Sievert apparatus

2.5.1 Apparatus

The Sievert experimental apparatus consists of various volumes, tubes, junctions, and valves (both manual and pneumatic), as well as temperature, pressure, and flow sensors. The detailed description of the components includes:

- Calibration Volume: A 50 cm^3 cylinder, thermally insulated can be separated from the system using a manual valve. This volume serves various purposes, such as increasing the total system volume during kinetic measurements.
- Expansion Volume: This volume, also known as the expansion lung, is connected to the system via a pneumatic valve and is used during the gas evacuation phase. A rotary vacuum pump maintains the volume under dynamic vacuum to facilitate filling or emptying.
- Sample Environment: The metallic sample is placed inside a cylinder with a lid equipped with a filter to prevent material leakage during filling and emptying phases. This environment is enclosed in a sample chamber made of stainless steel, with silver-coated seals to ensure optimal sealing. A thermocouple monitors the sample's temperature.
- Furnace: A cylindrical furnace made of ceramic material is used to heat the sample to the desired temperature. The temperature can be set via software or controlled externally through a display.
- Pressure Sensors: There are two pressure sensors: one located on the cross volume of the system and the other on the expansion lung. The first sensor provides a precision of 0.1% and is crucial for calculating the moles of gas absorbed or desorbed. The second sensor monitors the vacuum state in the expansion lung.
- Flowmeter and Thermocouples: The flowmeter, calibrated specifically for molecular hydrogen, measures the gas flow. Two type K thermocouples monitor the temperature in the sample chamber and the calibration volume. Both thermocouples are connected to a measurement system with a sensitivity of ±1°C and can operate across a wide temperature range.
- Flow Control Valves and Pneumatic Valves: Flow control valves MV1 and MV2, positioned on the gas inlet and outlet lines, respectively, regulate the gas flow, influencing internal pressure. Pneumatic valves PV1, PV2, and PV3, activated by solenoid valves, control gas flow within the apparatus, allowing pressure adjustment at various points in the system without affecting the sample chamber.

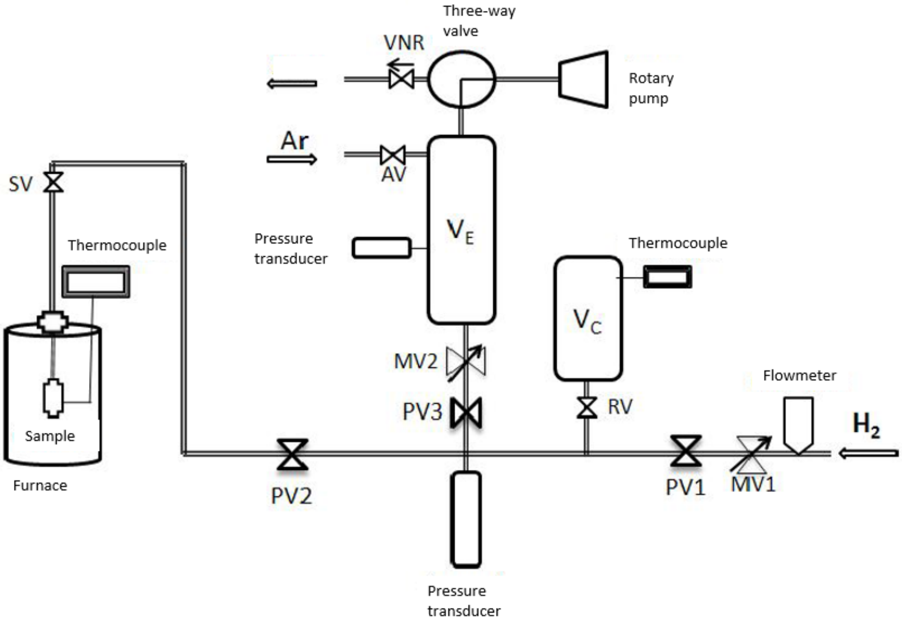

Figure 2.12: Sievert apparatus

2.5.2 Volumes calibration

In light of the frequent reliance on volume values within the apparatus for various calculations, achieving a high level of precision in their determination becomes a fundamental requirement. To accomplish this, we employ a method involving free gas expansions at room temperature for volume calibration. First, we set an initial pressure (P_i) throughout the entire system. Following this, we close the RV valve and proceed to evacuate the remaining system until a vacuum is achieved. Afterward, we close both the PV2 and SV valves.

Next, we open the RV valve and measure the final pressure (P_f) that is reached. This same step is repeated for the PV2 and SV valves. It is worth noting that it is essential to allow some time for the gas to rethermalize after the valves are opened in order to stabilize the pressure.

The equation we employ in this process is Boyle's law for isothermal transformations: $P_iV_i = P_fV_f$. By referencing the known calibration volume (V_C), one can sequentially derive the values of all other volumes:

$$V_f = \frac{P_i}{P_f} \cdot V_i \tag{2.3}$$

The volumes that have been found are in table 2.2.

Volume Symbol	Value (cm^3)
VC	51.20 ± 0.10
VX	17.11 ± 0.04
VT	2.52 ± 0.06
VSH	6.11 ± 0.06

Table 2.2: Summary of Instrument Volumes.

2.5.3 The sample environment

The metal sample is placed inside a cylinder with a lid equipped with a filter to prevent material leakage during the emptying and filling phases. The entire setup is housed within a sample chamber consisting of various parts, as shown in Figure 2.13. All the components are made of stainless steel and suitable for working in pressurized environments with high temperatures. The seals used, as well as the threads, are coated with a layer of silver that acts as a lubricant. The gasket between the body and the female nut must be replaced after each opening of the chamber to ensure optimal sealing performance. A thermocouple in contact with the chamber communicates the current temperature to the software, which can also be displayed on a dedicated external screen. The sample chamber is welded to a stainless steel tube with a diameter of 1/4” to facilitate its positioning inside the furnace. Communication with the rest of the system is ensured by a manual SV valve connected to a capillary tube leading to PV2.

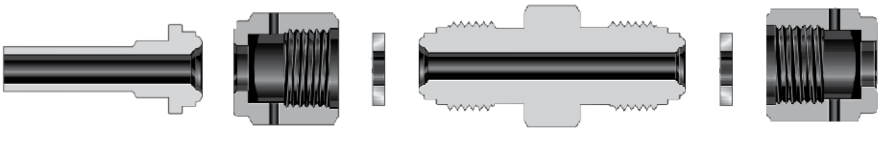

Figure 2.13: Sample holder

2.5.4 The volumetric method

The Sievert apparatus used for these measurements consists of a series of tubes that connect, through manual or pneumatic valves, a main hydrogen reservoir, referred to as the calibration volume, to the sample-carrying chamber positioned inside a furnace. The system is equipped with sensors for temperature and pressure monitoring and setting, as well as a gas injection and evacuation system, which can be either hydrogen or argon.

The volumetric method for calculating the quantity of hydrogen absorbed or desorbed from the sample relies on the ideal gas equation. Assuming that the fixed-volume system

V is initially at temperature T and pressure P_i, the absorption/desorption of hydrogen leads to an initial pressure change $dP = P_f - P_i$, negative for absorptions and positive for desorptions. This pressure change allows us to determine the number of moles of hydrogen $dn = n_f - n_i$ absorbed/desorbed by the sample:

$$dn = n_f - n_i = \frac{V}{RT}(P_f - P_i) = \frac{V}{RT}dP \tag{2.4}$$

By knowing the molecular weight of hydrogen M_{H_2} (2.01594 g/mol), we can then determine the mass of the absorbed gas m_{H_2} as:

$$m_{H_2} = M_{H_2} \cdot dn = \frac{M_{H_2}}{V} \cdot RT \cdot dP \tag{2.5}$$

However, it is more convenient to express the amount of hydrogen stored by the metal as a ratio between the mass of absorbed hydrogen m_H and the total mass of the sample, which includes both the metal and the hydrogen inside it. This quantity, referred to as weight percent (wt%), is the one most commonly reported on the P-C graphs:

$$wt\% = \frac{m_{Hydride}}{m_H} \cdot 100 \tag{2.6}$$

The use of the ideal gas equation is justified by the typical pressure range of such an apparatus, which is 0-20 bar, well below the critical pressure of 5 MPa. Beyond this point, the behavior of real gases starts to manifest, as described by the Van der Waals equation:

$$P + \frac{a}{V^2 m}(V_m - b) = RT \tag{2.7}$$

Here, 'a' (0.2476 L^2 bar mol^{-2}) and 'b' (0.02661 L mol^{-1}) are constants characteristic of hydrogen atoms and measure the extent of their mutual attraction and their volume, respectively. V_m represents the molar volume.

2.5.5 Sources of errors for the volumetric method

Possible sources of errors that need to be taken into account during the design of a Sievert-type apparatus:

- Temperature Monitoring: Temperature monitoring is evidently important in the construction of a Sievert apparatus. In general, the further the sample's temperature is from the temperature of the chamber containing the sample, the more relevant the issue of thermal gradients in the system becomes. Naturally, a poorly thermostated system would result in gross measurement errors regardless of the sample's temperature. Unlike in thermogravimetric analyses, in the case of a volumetric apparatus, temperature can be measured by placing a thermocouple in contact with the sample, allowing close monitoring of the temperature variations it undergoes. This helps control the issue of samples undergoing endothermic or exothermic reactions during hydride formation. Absorption measurements must be conducted under conditions of thermal equilibrium. By closely monitoring any temperature variations in the sample due to significant heat release or absorption, it can be ensured that the sample is also in thermal equilibrium. Of course, the relevance of this phenomenon depends on the nature and size of the sample. Another issue related to temperature monitoring is the potential presence of ”cold spots” and ”hot spots” in the system, which respectively lead to false absorption and desorption measurements. Once again, it is important to have a properly thermostated system.

- Gas Purity: Additional considerations need to be made regarding the purity of the gas introduced into the system. Typically, intrinsic impurities can be reduced to parts per million using a reliable in-situ filtration method (useful if the hydrogen supply is not directly connected to the instrument). Any impurities present in the system due to air ingress during sample loading procedures tend to absorb the gas themselves, disturbing the measurement, or they can interact with the sample's surface, hindering the dissociation of molecular hydrogen and potentially causing irreparable damage to particularly delicate samples. To address this issue, it is necessary to minimize the system's contact with air as much as possible and establish a purification procedure using inert gases such as argon.
- Internal Volumes of the Apparatus: Since the Sievert method relies on measuring pressure variations of hydrogen gas in a fixed volume to determine the amount of hydrogen absorbed or desorbed by a sample, it is crucial for the volume of a volumetric apparatus to be appropriately sized for detection. Additionally, the apparatus volume must be sufficiently large so that the pressure change resulting from hydrogen absorption or desorption does not halt the process before complete hydrogenation or dehydrogenation of the sample is achieved, especially when aiming to measure the kinetics of desorption. This problem can be addressed in part by employing a high-quality pressure sensor, selecting sample sizes that allow for detectable pressure changes due to hydrogen absorption (or desorption), or reducing the system volumes to enable analysis of smaller samples. The alternative that offers the greatest versatility of the instrument is the use of a variable system volume (with the possibility of excluding calibrated volumes) depending on the size and properties of the sample to be characterized.
- Sample History: The history of treatments that the sample has undergone and the conditions in which it has been prepared are important factors that can undermine not only the accuracy of the measurement but also its validity. The significance of this issue can vary greatly depending on the material. A clarifying example

is that of microporous absorbents, which must be properly degassed before being subjected to analysis.

- Pressure Leakage: Preventing significant pressure leakage from the instrument is crucial to avoid gross measurement errors. The choice of joints, tubes, and valves used to construct the system must be made considering their operating limits of pressure and temperature. Additionally, a procedure needs to be established to check for any leakage resulting from improper assembly of the system during sample loading.

2.6 Pressure-Composition Isotherms

The Pressure-Composition Isotherms, or PCIs, are the most commonly used methods for determining the thermodynamics of the system in question. They are represented by a collection of data points indicating the pressure and concentration of a sample at equilibrium, highlighting the relationships between the thermodynamic variables influencing concentration. The two critical pieces of information that can be extracted from these measurements are the plateau pressure at which the phase transition occurs from separate hydrogen and metal to hydride, and the maximum achievable hydrogen concentration. A proper interpretation of the data from a PCI, especially the equilibrium pressure, must consider two fundamental aspects: the first is that experimentally, it is impossible to reach true thermodynamic equilibrium conditions since the system's pressure asymptotically approaches equilibrium, taking theoretically infinite time; the second is due to the hysteresis loop exhibited by the P-C curve during absorption and desorption. Generally, it is observed that the hydrogenation phase occurs at slightly higher pressures compared to the dehydrogenation phase. This behavior is due to the hydrogen's need to deform the crystal lattice of the metal before it can penetrate it, causing an excess pressure during absorption that does not manifest during desorption.

It is useful to delve into the relationship between a PCI and kinetics: when a sample is perturbed by a pressure change, the system tends to reach a new equilibrium through a dynamic process typical of a kinetic measurement. The final data point of each kinetics, which likely represents the new thermodynamic equilibrium, provides a unique set of pressure and concentration values for the PCI. To obtain a curve on the pressure-temperature graph, it is necessary to conduct numerous kinetics at the same temperature. The plateau pressure is usually indicated as the average between the absorption and desorption pressures.

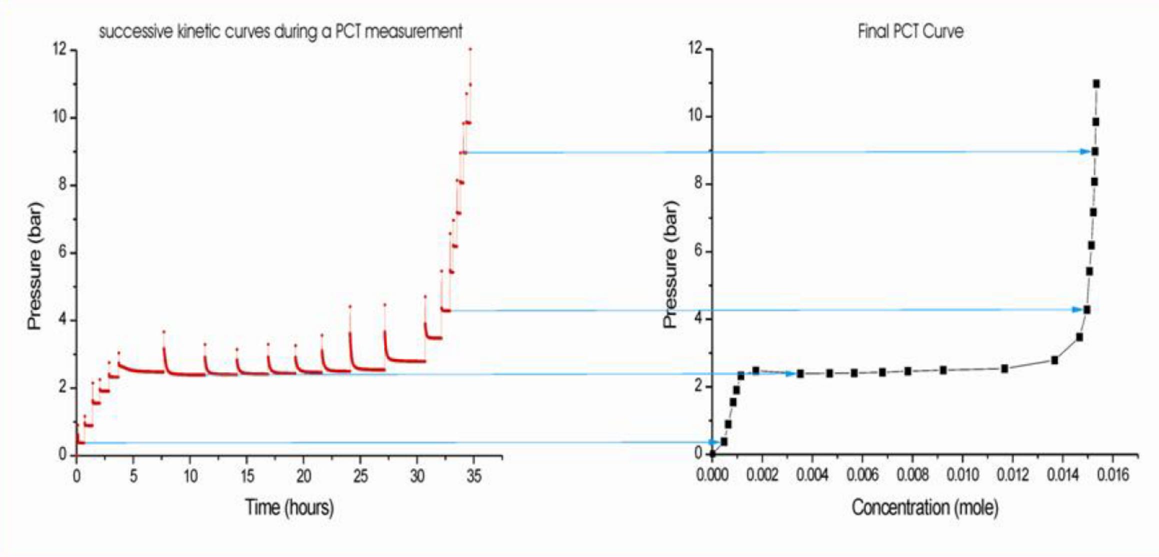

Figure 2.14: Relation between Kinetics and PCI

Chapter 3

Results and Discussion

3.1 Synthesis of the materials by RBM

The parameter of the milling of all the materials were the same, they were milled at 600rpm alternating periods of milling of 3 minutes at periods of pause of 9 minutes, all was repeated for 100 cycles. From the graph in Figure 3.1 is possible to observe that the absorption of hydrogen in sample A occurred in two steps. Hydrogen absorption reaction by magnesium (Mg):

$$Mg + H_2 \rightarrow MgH_2 \tag{3.1}$$

Reaction between magnesium hydride (MgH_2), iron (Fe) and H_2 to form the compound Mg_2FeH_6:

$$2MgH_2 + Fe + H_2 \rightarrow Mg_2FeH_6 \tag{3.2}$$

It is important to note that the reactive ball milling process, which combines high-energy mechanical milling with the chemical reaction, enhances the reaction kinetics, promoting hydrogen absorption by magnesium and subsequent reaction with iron to form the Mg_2FeH_6 compound.

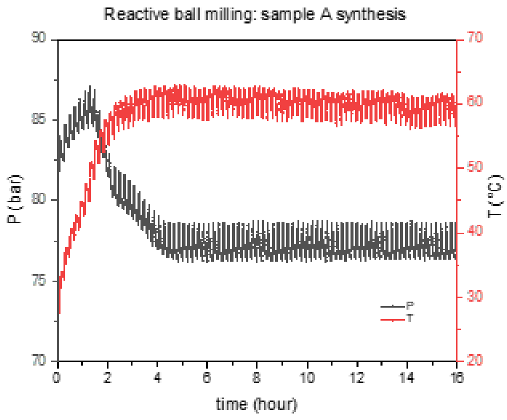
Reactive ball milling: sample A synthesis
P (bar)
T (°C)
time (hour)
P
T
90
85
80
75
70
70
60
50
40
30
20
0
2
4
6
8
10
12
14
16

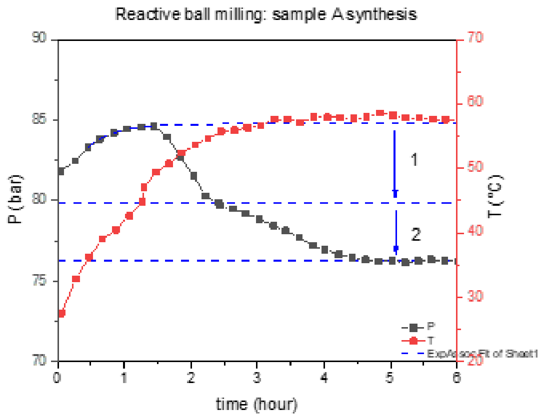
Reactive ball milling: sample A synthesis
P (bar)
T (°C)
time (hour)
1
2
P
T
ExpAssoc Fit of Sheet1
90
85
80
75
70
70
60
50
40
30
20
0
1
2
3
4
5
6

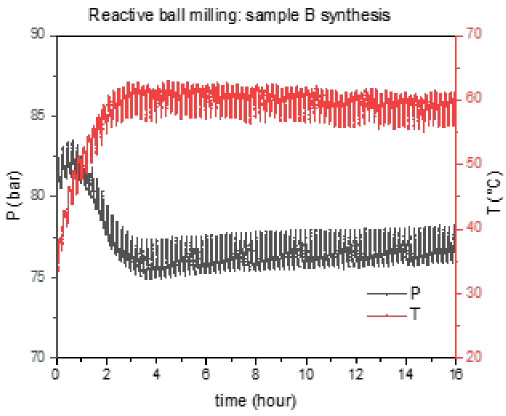
Reactive ball milling: sample B synthesis
P (bar)
T (°C)
time (hour)
P
T
90
85
80
75
70
70
60
50
40
30
20
0
2
4
6
8
10
12
14
16

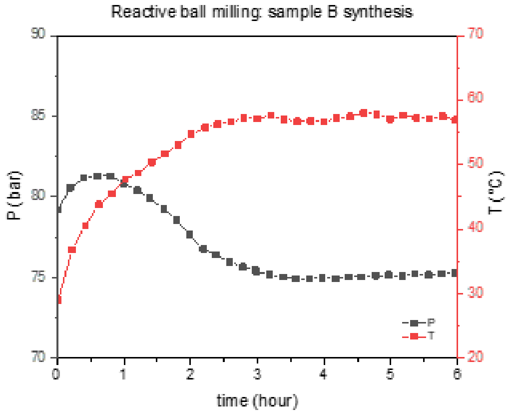
Reactive ball milling: sample B synthesis
P (bar)
T (°C)
time (hour)
P
T
90
85
80
75
70
70
60
50
40
30
20
0
1
2
3
4
5
6

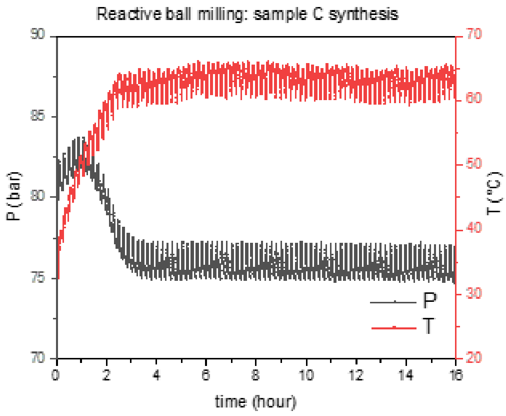
Reactive ball milling: sample C synthesis
P (bar)
T (°C)
time (hour)
P
T
90
85
80
75
70
70
60
50
40
30
20
0
2
4
6
8
10
12
14
16

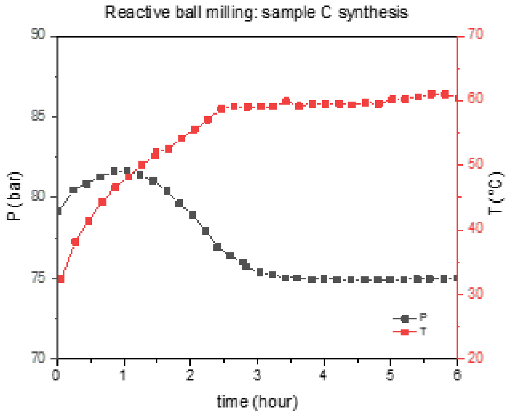
Reactive ball milling: sample C synthesis
P (bar)
T (°C)
time (hour)
P
T
90
85
80
75
70
70
60
50
40
30
20
0
1
2
3
4
5
6

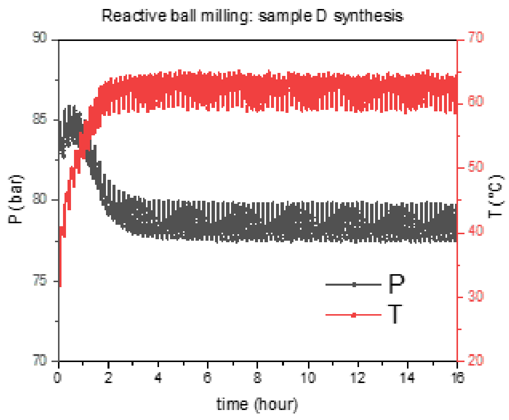
Reactive ball milling: sample D synthesis
P (bar)
T (°C)
time (hour)
P
T
70
75
80
85
90
20
30
40
50
60
70
0
2
4
6
8
10
12
14
16

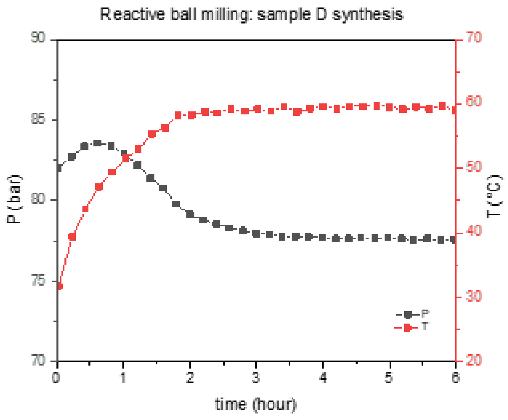
Reactive ball milling: sample D synthesis
P (bar)
T (°C)
time (hour)
P
T
70
75
80
85
90
20
30
40
50
60
70
0
1
2
3
4
5
6

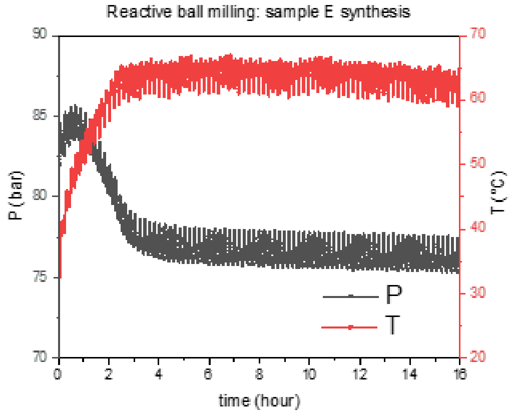
Reactive ball milling: sample E synthesis
P (bar)
T (°C)
time (hour)
P
T
70
75
80
85
90
20
30
40
50
60
70
0
2
4
6
8
10
12
14
16

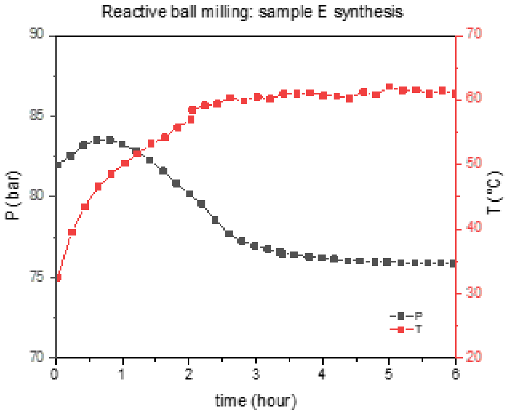
Reactive ball milling: sample E synthesis
P (bar)
T (°C)
time (hour)
P
T
70
75
80
85
90
20
30
40
50
60
70
0
1
2
3
4
5
6

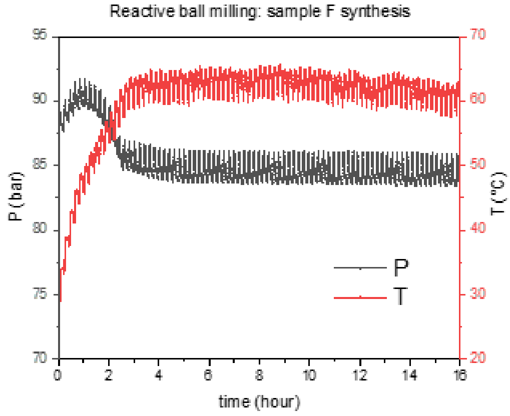
Reactive ball milling: sample F synthesis
P (bar)
T (°C)
time (hour)
P
T
70
75
80
85
90
95
20
30
40
50
60
70
0
2
4
6
8
10
12
14
16

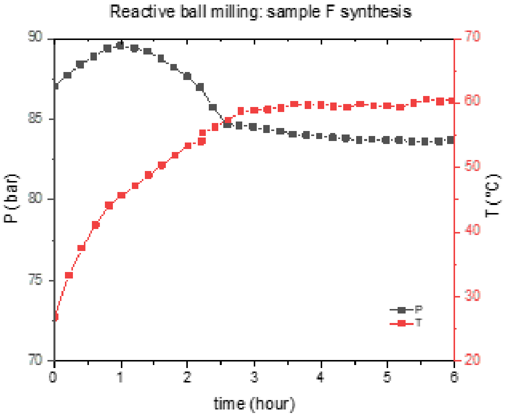
Reactive ball milling: sample F synthesis
P (bar)
T (°C)
time (hour)
P
T
70
75
80
85
90
20
30
40
50
60
70
0
1
2
3
4
5
6

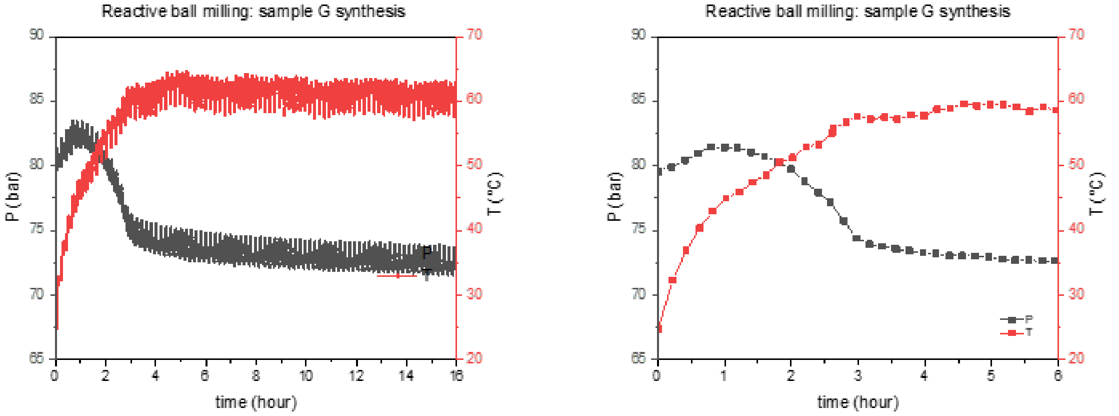

Figure 3.1: Reactive ball milling synthesis on the left the raw data taken during RBM, on the right the points of the data taken at the end of each 3 minutes cycle, a)sample A, b)sample B, c)sample C, d)sample D , e)sample E, f)sample F, g) sample G

During the synthesis we can evaluate from the pressure drop in the vial the number of hydrogen atoms absorbed by the reactants per targeted metal unit formula (H/u.f.) as well as by the weight percent (wt%). These values are gathered in table 3.1.

Table 3.1: Comparison between hydrogen absorption during RBM and hydrogen desorption during TPD.

sample	Targeted sample composition	Initial metal reactants	Hydrogen uptake during RBM (H/u.f.)	Hydrogen uptake during RBM (wt%)	Hydrogen release during TPD (H/u.f.)	Hydrogen release during TPD (wt%)
A	Mg_2FeH_6	2 Mg + Fe	6.2 ± 0.3	5.7 ± 0.3	5.4 ± 0.3	4.9 ± 0.2
B	$Mg_2Fe_{0.5}Co_{0.5}H_x$	2 Mg + 0.5Fe + 0.5Co	3.5 ± 0.2	3.2 ± 0.2	3.7 ± 0.2	3.4 ± 0.2
C	$Mg_2Fe_{0.3}Co_{0.3}Ni_{0.3}H_x$	2 Mg + 0.3Fe + 0.3Co + 0.3Ni	4.0 ± 0.2	3.9 ± 0.2	4.3 ± 0.2	4.1 ± 0.2
D	$Mg_2Fe_{0.25}Co_{0.25}Ni_{0.25}Mn_{0.25}H_x$	2 Mg + 0.25Fe + 0.25Co + 0.25Ni + 0.25Mn	4.2 ± 0.2	3.9 ± 0.2	4.9 ± 0.2	4.5 ± 0.2
E	$Mg_3Fe_{0.25}Co_{0.25}Ni_{0.25}Mn_{0.25}H_x$	3 Mg + 0.25Fe + 0.25Co + 0.25Ni + 0.25Mn	6.6 ± 0.3	4.9 ± 0.2	6.4 ± 0.3	4.7 ± 2
F	$Mg_2Fe_{0.2}Co_{0.2}Ni_{0.2}Mn_{0.2}Cr_{0.2}H_x$	2 Mg + C.alloy	4.3 ± 0.2	3.8 ± 0.2	4.4 ± 0.2	3.9 ± 0.2
G	$Mg_3Fe_{0.2}Co_{0.2}Ni_{0.2}Mn_{0.2}Cr_{0.2}H_x$	3 Mg + C.alloy	7.4 ± 0.4	5.5 ± 0.3	6.8 ± 0.3	5.0 ± 0.3

The amount of hydrogen content uptake during RBM and the one released during TPD should be in the ideal case identical, this would mean a perfect reversibility of the reaction. In the case of sample A, E and G the amount of hydrogen releasd is less than the one uptake, this can be index of a not total reversibility of the reaction. In the case of sample B, C and F it is possible to observe that the amount of hydrogen released in higher than the one uptake in absolute value but considering the errors associated to both de measures the reliability of the values can be considered acceptable. In sample D it is also possible to observe that even considering the errors associated to the two values the amount of hydrogen uptake is less than the one release, this can be due to a possible overestimation to the error associated to the measures that was considered 5%.

3.2 XRD after Synthesis

After analyzing the X-ray diffraction patterns obtained post-synthesis, it is evident that the peaks observed in the different materials are remarkably similar. This observation leads us to conclude that predominantly a K_2PtCl_6 crystal structure has been formed. This category includes crystals that exhibit the Fm$\bar{3}$m space group symmetry (No. 225) within the cubic crystal system (Figure 3.2). For Mg_2FeH_6, Mg, Fe, and H atoms occupy the same atomic positions as K, Pt, and Cl, respectively.

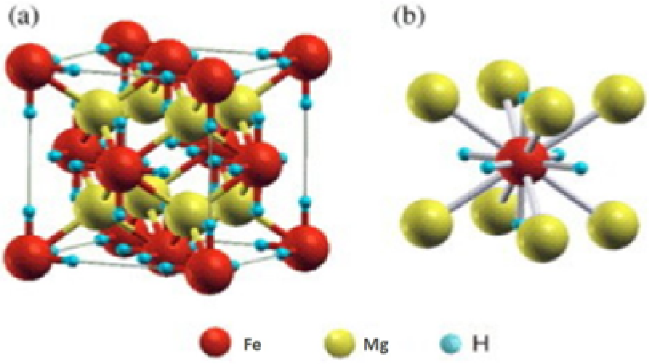

Figure 3.2: The crystal structure of (a)Mg_2FeH_6 and (b) atomic coordination around Fe atoms

The other diffraction lines observed in hydrogenation compounds can be indexed according to two space groups: either Im$\bar{3}$m, which represents a cubic crystal structure with inversion symmetry, or P63/mmc, which represents a hexagonal crystal structure with additional symmetry elements.

In Figure 3.3, it is possible to distinguish peaks at $2\theta = 27.5°$, 46°, 54°, 67°, and 85.5° that are present in all XRD patterns. They can all be indexed to the K_2PtCl_6 type structure. However, additional peaks are found in all patterns. We will now comment on the assessment of each individual case according to phase identification from EVA software and the fit of diffraction patterns using Rietveld analysis by Full Proof Suite software. The determined crystallographic data is given in Table 3.2.

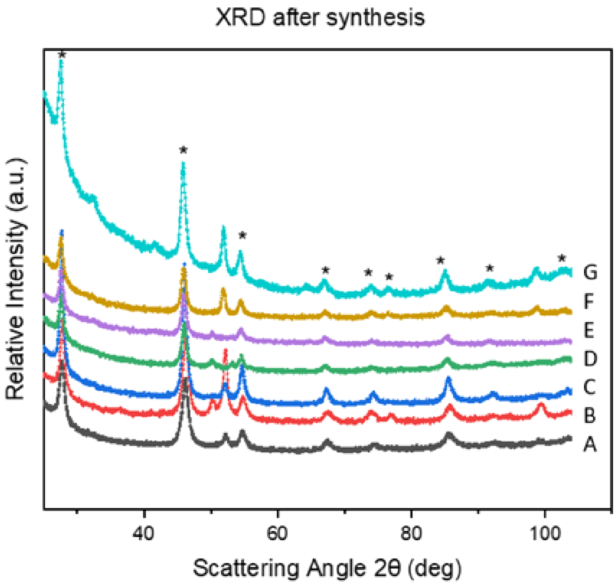

Figure 3.3: Comparison of all the XRD patterns. Peaks belonging to the K_2PtCl_6 type structure are indicated with asterisks (*).

Table 3.2: Results of Rietveld analysis of the samples after synthesis

Sample	**Phases**	**Space group**	**Structure type**	**Weight fraction (%)**	**Cell parameters**			**Cell volume**
					a	**b**	**c**	
A	Mg_2FeH_6	$Fm\bar{3}m$	FCC	95.5	6.44232	6.44232	6.44232	267.379
	Fe	$Im\bar{3}m$	BCC	4.5	2.87253	2.87253	2.87253	23.703
B	$Mg_2Fe_{0.5}Co_{0.5}H_{5.5}$	$Fm\bar{3}m$	FCC	76.33	6.44157	6.44157	6.44157	267.285
	Fe	$Im\bar{3}m$	BCC	18.66	2.87579	2.87579	2.87579	23.783
	MgCo	$Im\bar{3}m$	BCC	5.01	2.97707	2.97707	2.97707	26.386
C	$Mg_2Fe_{0.25}Co_{0.25}Ni_{0.25}Mn_{0.25}H_x$	$Fm\bar{3}m$	FCC	95.58	6.45247	6.45247	6.45247	268.645
	Fe	$Im\bar{3}m$	BCC	4.42	2.87715	2.87715	2.87715	23.817
D	$Mg_2Fe_{0.25}Co_{0.25}Ni_{0.25}Mn_{0.25}H_x$	$Fm\bar{3}m$	FCC	89.95	6.46766	6.46766	6.46766	270.546
	MgCo	$Im\bar{3}m$	BCC	1.18	3.01043	3.01043	3.01043	27.283
	Mn	P4132	Tetragonal	8.87	6.31958	6.31958	6.31958	252.385
E	$Mg_3Fe_{0.25}Co_{0.25}Ni_{0.25}Mn_{0.25}H_x$	$Fm\bar{3}m$	FCC	88.65	6.47083	6.47083	6.47083	270.944
	Mn	P4132	Tetragonal	3.13	6.32080	6.32080	6.32080	252.532
	MgH_2	P42/mnm	Tetragonal	8.22	4.50429	4.50429	3.00509	60.969
F	$Mg_2Fe_{0.2}Co_{0.2}Ni_{0.2}Mn_{0.2}Cr_{0.2}H_x$	$Fm\bar{3}m$	FCC	87.42	6.47392	6.47392	6.47392	271.332
	Fe	$Im\bar{3}m$	BCC	12.58	2.88796	2.88796	2.88796	24.086
G	$Mg_3Fe_{0.2}Co_{0.2}Ni_{0.2}Mn_{0.2}Cr_{0.2}H_x$	$Fm\bar{3}m$	FCC	73.12	6.48039	6.48039	6.48039	272.147
	Fe	$Im\bar{3}m$	BCC	9.45	2.88739	2.88739	2.88739	24.072
	MgH_2	P42/mnm	Tetragonal	17.43	4.50063	4.50063	3.02521	61.278

As it is possible to conclude observing Table 3.2 that for samples A, B, C, F and G the targeted hydrides, discussed in Table 2.1, were formed during RBM with weight fractions that varies from 95% to 73%. In particular considering samples E and G, that have 3 atoms of Mg, it is possible to conclude that both formed a lower amount of hydride compared to the corresponding samples D and F that have 2 atoms of Mg. This is reasonable since it was detected the formation of MgH_2 in both cases. Considering samples D and E is not sure that the hydrides targeted were fully formed because it is possible to see that part of the total amount of Mn (8 and 3 percent of the total weight) was not used to create the targeted hydrides. Infact in the case of sample D the initial average weight of Mn in the sample was 10,5% so if a 8% remains unused during RBM this is a considerable big part. In the second case the average weight percent of Mn before the milling was 8,5% so we can conclude that since just only a 3% remains after the RBM the targeted compound was formed.

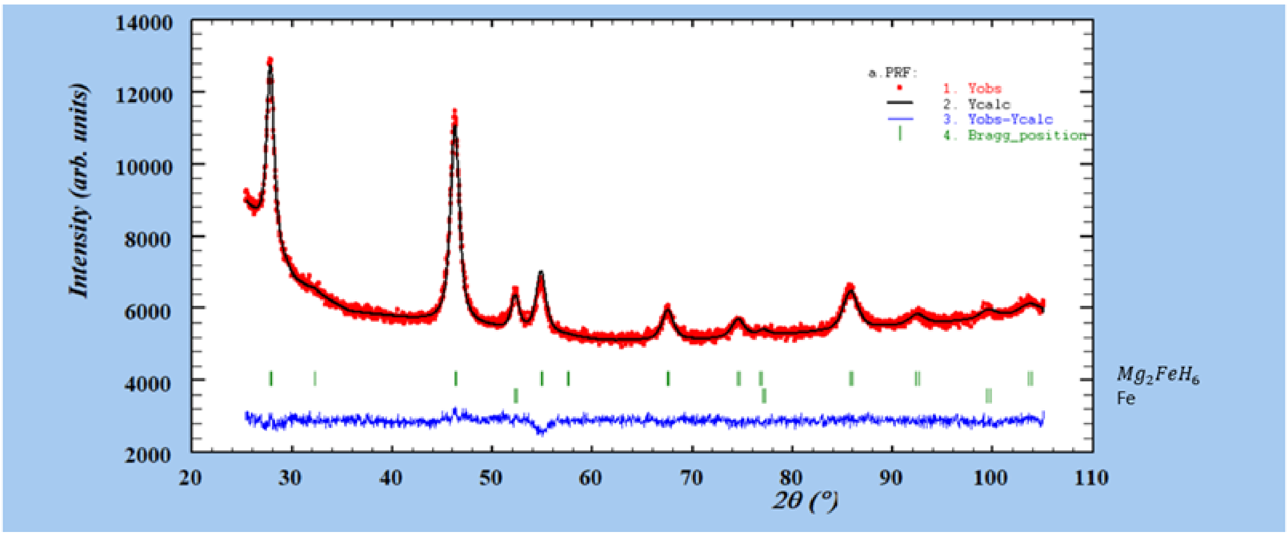

Intensity (arb. units)
14000
12000
10000
8000
6000
4000
2000
20
30
40
50
60
70
80
90
100
110
2θ (°)
a.PRF:
1. Yobs
2. Ycalc
3. Yobs-Ycalc
4. Bragg_position
Mg_2FeH_6
Fe

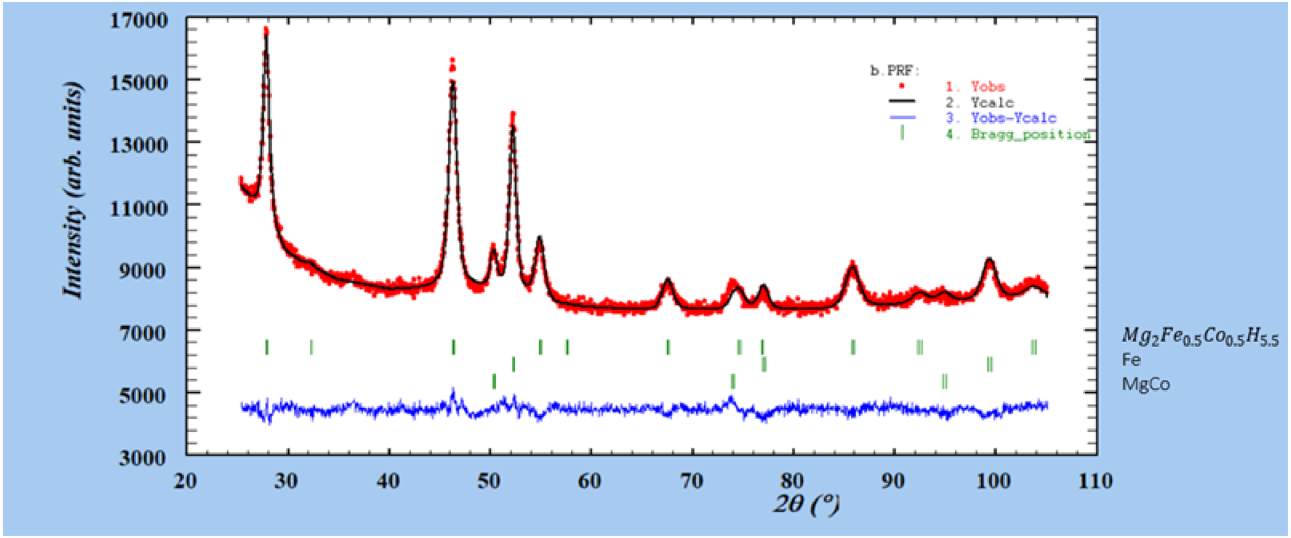

Intensity (arb. units)
17000
15000
13000
11000
9000
7000
5000
3000
20
30
40
50
60
70
80
90
100
110
2θ (°)
b.PRF:
1. Yobs
2. Ycalc
3. Yobs-Ycalc
4. Bragg_position
$Mg_2Fe_{0.5}Co_{0.5}H_{5.5}$
Fe
MgCo

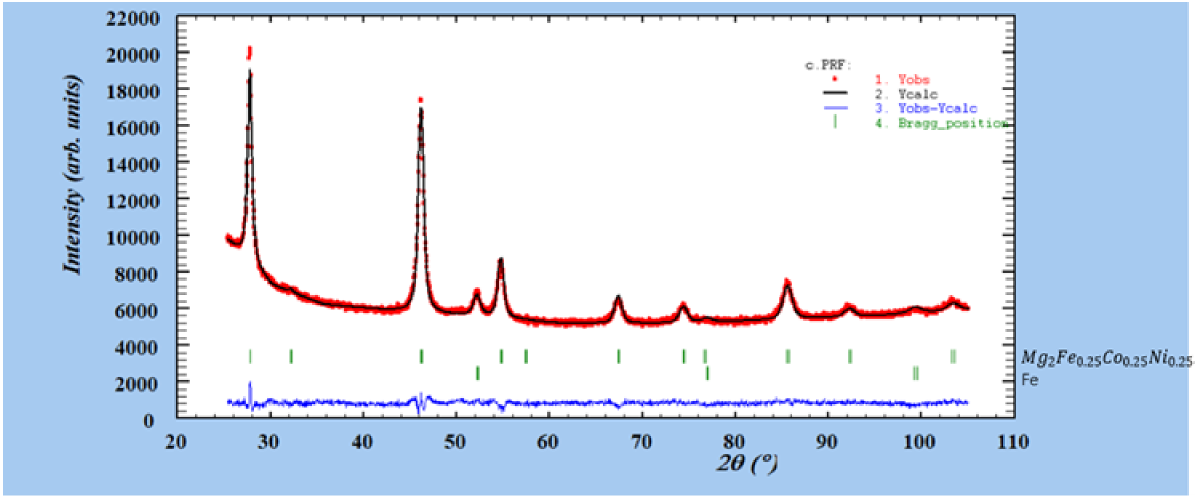

Intensity (arb. units)
22000
20000
18000
16000
14000
12000
10000
8000
6000
4000
2000
0
20
30
40
50
60
70
80
90
100
110
2θ (°)
c.PRF:
1. Yobs
2. Ycalc
3. Yobs-Ycalc
4. Bragg_position
$Mg_2Fe_{0.25}Co_{0.25}Ni_{0.25}Mn_{0.25}H_x$
Fe

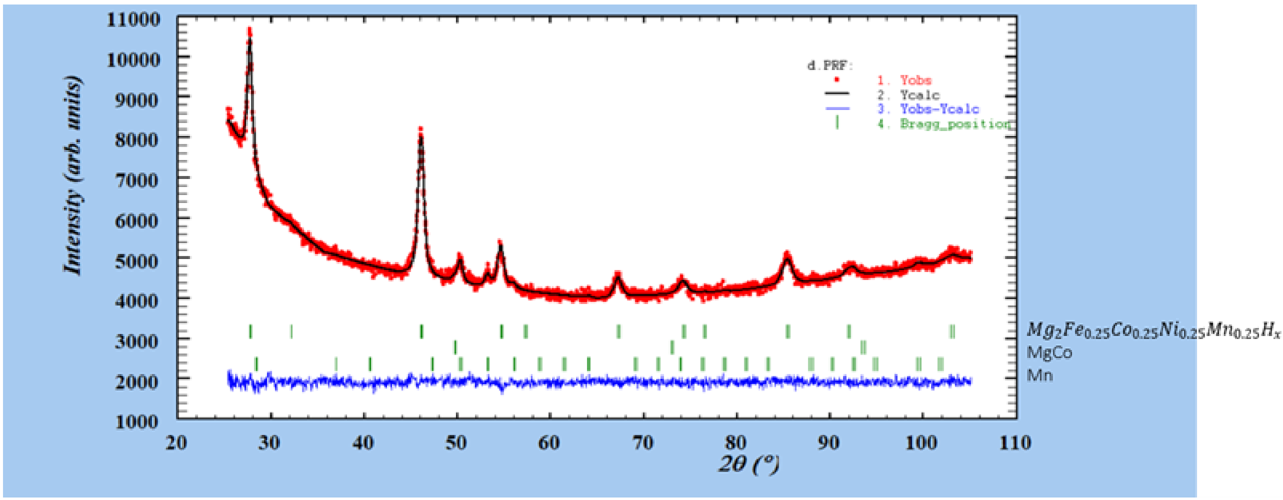
Intensity (arb. units)
11000
10000
9000
8000
7000
6000
5000
4000
3000
2000
1000
20
30
40
50
60
70
80
90
100
110
2θ (°)
d.PRF:
1. Yobs
2. Ycalc
3. Yobs-Ycalc
4. Bragg_position
$Mg_2Fe_{0.25}Co_{0.25}Ni_{0.25}Mn_{0.25}H_x$
MgCo
Mn

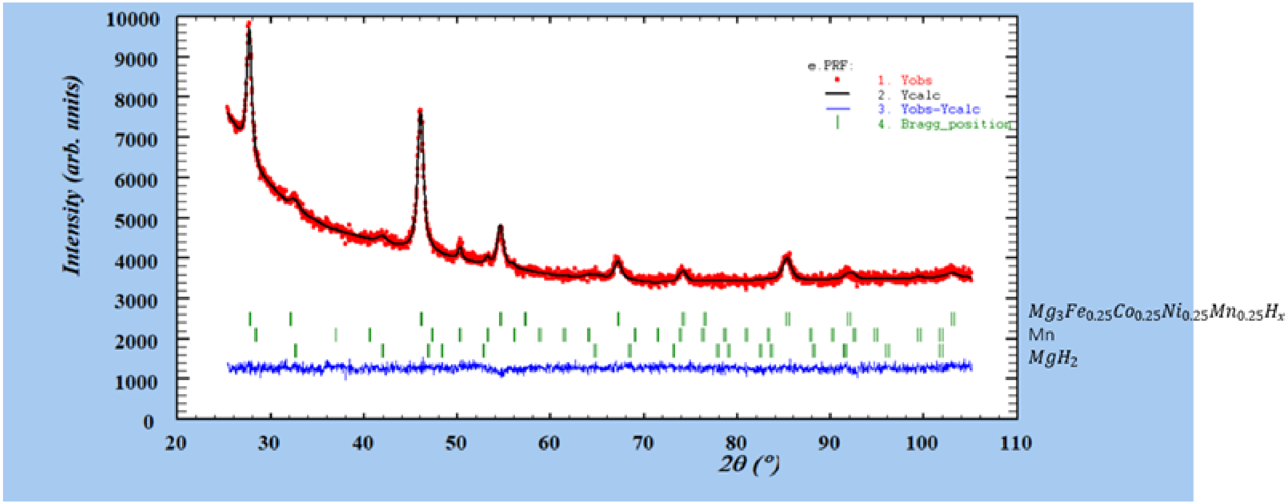
Intensity (arb. units)
10000
9000
8000
7000
6000
5000
4000
3000
2000
1000
0
20
30
40
50
60
70
80
90
100
110
2θ (°)
e.PRF:
1. Yobs
2. Ycalc
3. Yobs-Ycalc
4. Bragg_position
$Mg_3Fe_{0.25}Co_{0.25}Ni_{0.25}Mn_{0.25}H_x$
Mn
MgH_2

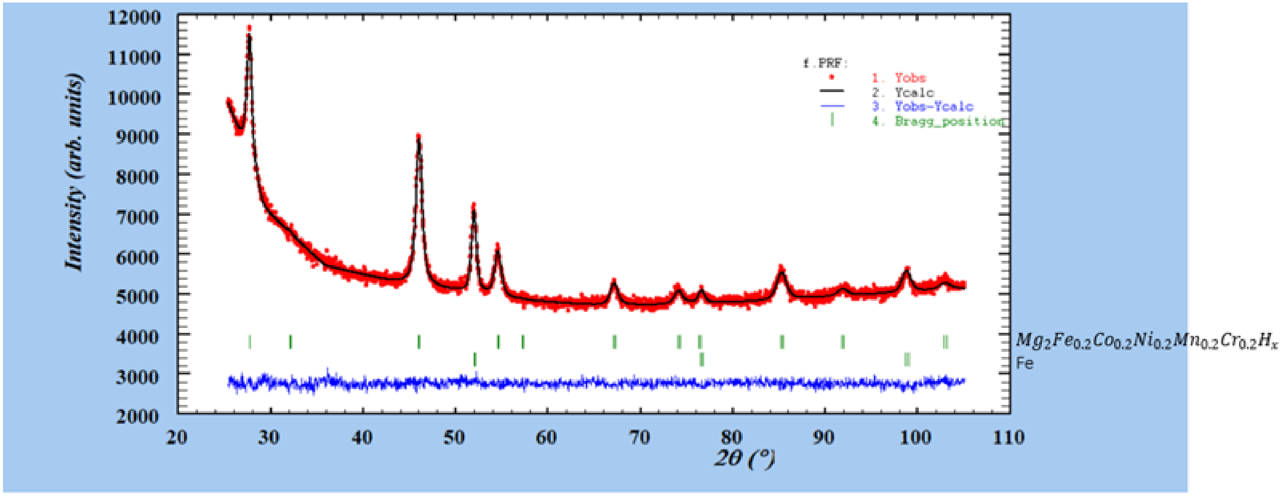
Intensity (arb. units)
12000
11000
10000
9000
8000
7000
6000
5000
4000
3000
2000
20
30
40
50
60
70
80
90
100
110
2θ (°)
f.PRF:
1. Yobs
2. Ycalc
3. Yobs-Ycalc
4. Bragg_position
$Mg_2Fe_{0.2}Co_{0.2}Ni_{0.2}Mn_{0.2}Cr_{0.2}H_x$
Fe

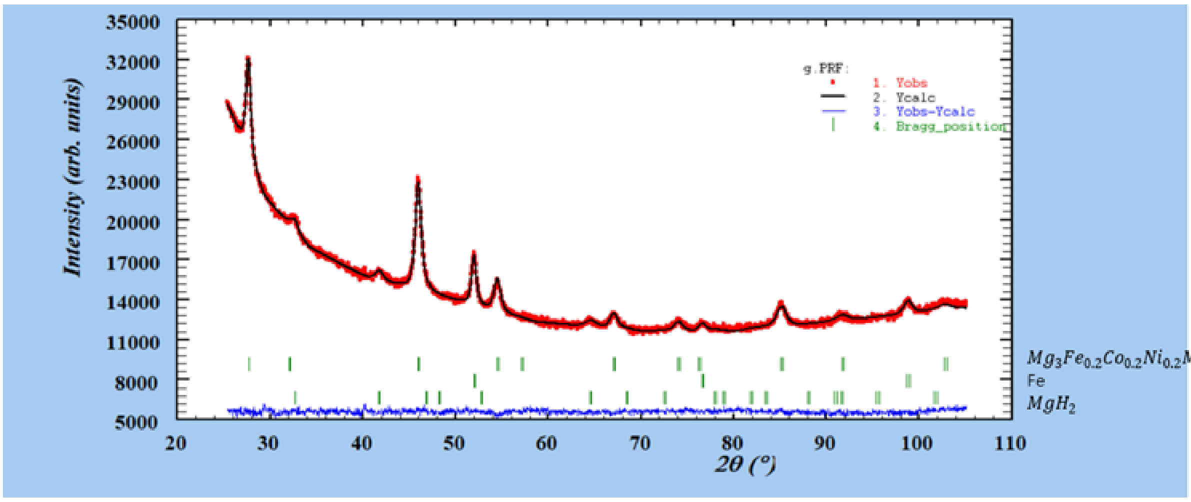

Figure 3.4: Reactive ball milling synthesis on the left the raw data taken during RBM, on the right the points of the data taken at the end of each 3 minutes cycle, a)sample A, b)sample B, c)sample C, d)sample D , e)sample E, f)sample F, g) sample G

3.3 Temperature Programmed Desorption (TPD)

A temperature programmed desorption was done to evaluate the thermal stability and total amount of hydrogen desorption as a function of temperature. The general trend of the curves clearly exhibits distinct patterns when divided into three regions based on temperature ranges. In the first region, spanning from 30°C to around 250°C, the pressure increase shows a relatively modest rise showing almost no hydrogen desorption. Moving on to the second region, encompassing temperatures from 250°C to 330°C, there is a notable and consistent high-pressure increase across all cases, indicating strong hydrogen release due to decomposition of hydride phases. Most prominently, the pressure increase within this range appears to follow a linear trajectory for the majority of samples. For the case of sample E and G, a dual-linear step is observed, implying that both samples contain two hydride phases that start desorbing at different temperature. Moving into the third region above 330°C, the pressure increase once again demonstrates a limited and steadier rise suggesting that samples are fully desorbed.

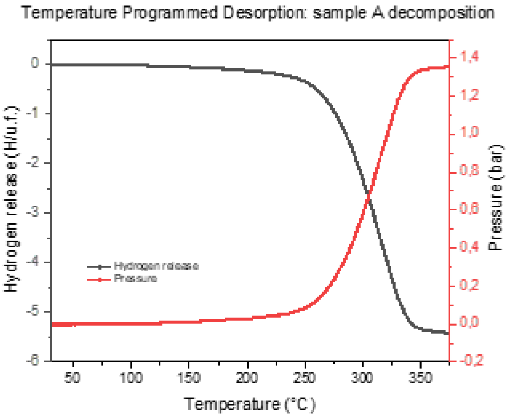
Temperature Programmed Desorption: sample A decomposition

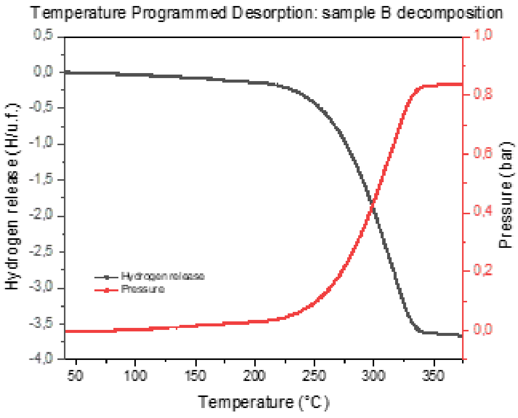
Temperature Programmed Desorption: sample B decomposition

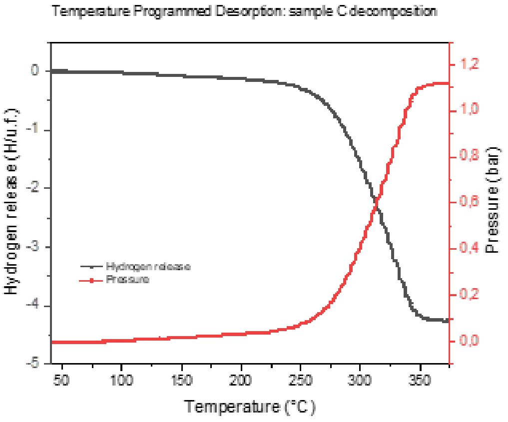
Temperature Programmed Desorption: sample C decomposition

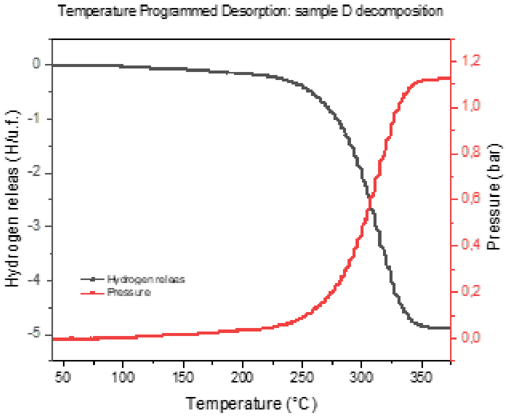
Temperature Programmed Desorption: sample D decomposition

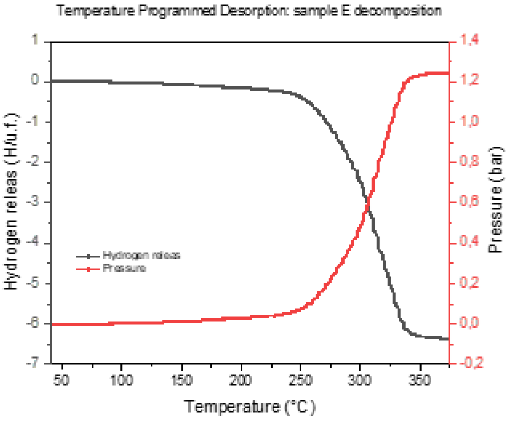
Temperature Programmed Desorption: sample E decomposition

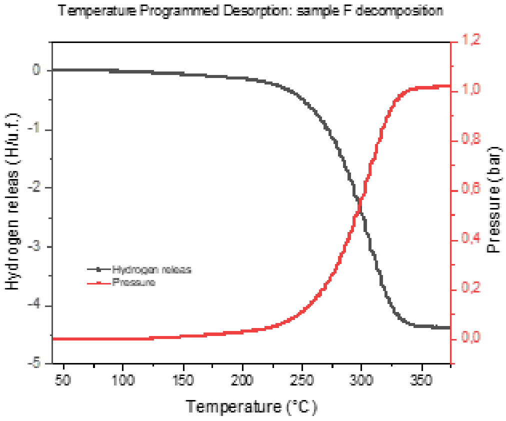
Temperature Programmed Desorption: sample F decomposition

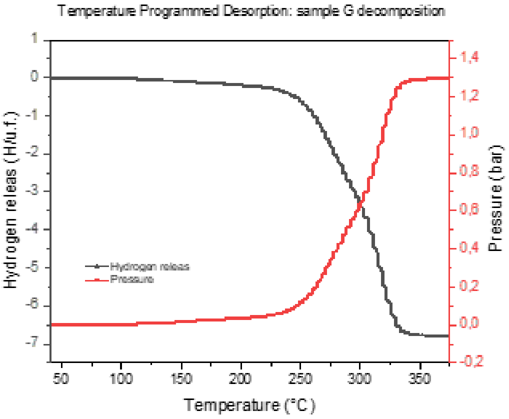

Figure 3.5: Temperature Programmed Desorption: a) Sample A, b) Sample B, c) Sample C, d) Sample D, e) Sample E, f) Sample F, g) Sample G

From the TPD, we can evaluate the total amount of hydrogen desorbed. It can be compared to the hydrogen content obtained by RBM experiments as shown in Table 3.1.

It was also possible to analyze the desorption temperature of the 7 samples using the tangent method to determine the onset temperature. Specifically, two linear fits were performed: the first for the initial behavior of the curve at low temperatures, and the second tangent to the curve during the typical desorption process. Then, using the equation of the two lines, the point of intersection was calculated, obtaining the onset temperature. For samples E and G, there were found two onset temperatures, one for the complex hydride and the other for the magnesium hydride. The values found are reported in Table 3.3. It is possible to observe that the values of onset temperatures do not vary substantially. Infact, starting from the known samples A and B the addition of TM do not follow a substantial change of onset temperature, so probably the kinetics process of desorption and the thermal stability remain similar for all the samples.

Table 3.3: Onset Temperatures of each sample

Sample	Onset Temperature (°C)
A	267
B	261
C	275
D	274
E	257 (Fit2) 273 (Fit3)
F	263
G	247 (Fit2) 277 (Fit3)

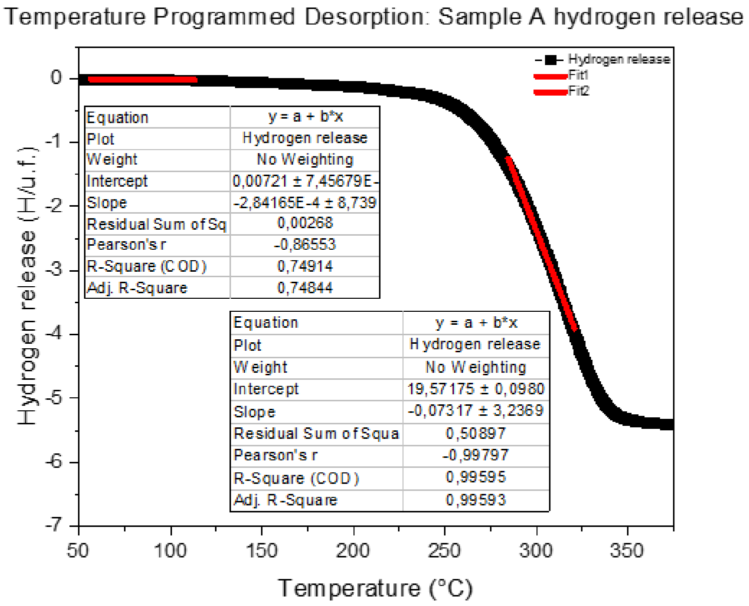
Temperature Programmed Desorption: Sample A hydrogen release

Equation	y = a + b*x
Plot	Hydrogen release
Weight	No Weighting
Intercept	0,00721 ± 7,45679E-
Slope	-2,84165E-4 ± 8,739
Residual Sum of Sq	0,00268
Pearson's r	-0,86553
R-Square (COD)	0,74914
Adj. R-Square	0,74844

Equation	y = a + b*x
Plot	Hydrogen release
Weight	No Weighting
Intercept	19,57175 ± 0,0980
Slope	-0,07317 ± 3,2369
Residual Sum of Squa	0,50897
Pearson's r	-0,99797
R-Square (COD)	0,99595
Adj. R-Square	0,99593

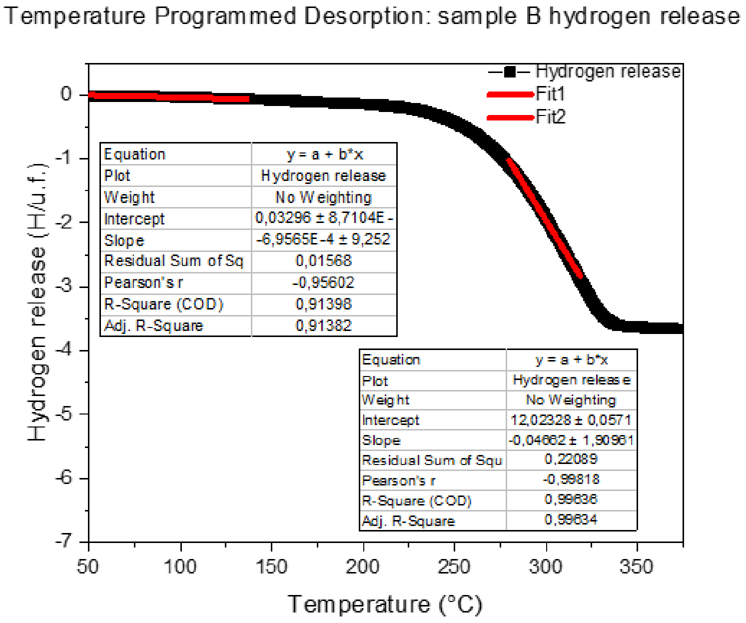
Temperature Programmed Desorption: sample B hydrogen release

Equation	y = a + b*x
Plot	Hydrogen release
Weight	No Weighting
Intercept	0,03296 ± 8,7104E-
Slope	-6,9565E-4 ± 9,252
Residual Sum of Sq	0,01568
Pearson's r	-0,95602
R-Square (COD)	0,91398
Adj. R-Square	0,91382

Equation	y = a + b*x
Plot	Hydrogen release
Weight	No Weighting
Intercept	12,02328 ± 0,0571
Slope	-0,04662 ± 1,90961
Residual Sum of Squ	0,22089
Pearson's r	-0,99818
R-Square (COD)	0,99636
Adj. R-Square	0,99634

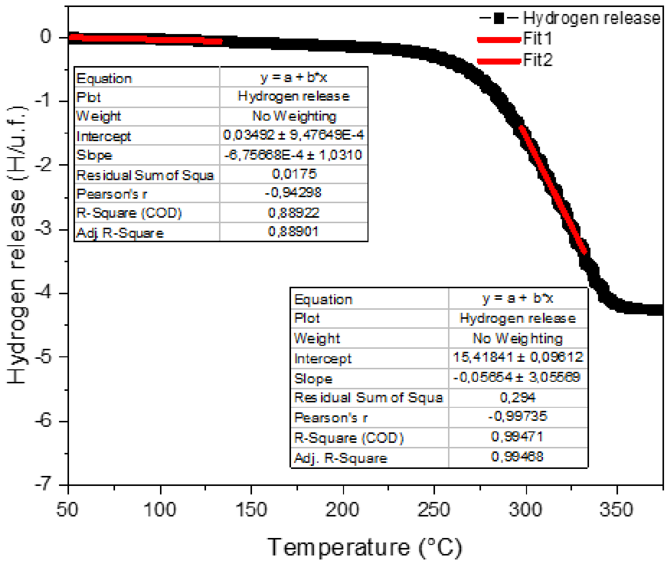
Temperature Programmed Desorption: Sample C hydrogen release

Equation	y = a + b*x
Plot	Hydrogen release
Weight	No Weighting
Intercept	0,03492 ± 9,47649E-4
Slope	-6,75668E-4 ± 1,0310
Residual Sum of Squa	0,0175
Pearson's r	-0,94298
R-Square (COD)	0,88922
Adj. R-Square	0,88901

Equation	y = a + b*x
Plot	Hydrogen release
Weight	No Weighting
Intercept	15,41841 ± 0,09612
Slope	-0,05654 ± 3,05569
Residual Sum of Squa	0,294
Pearson's r	-0,99735
R-Square (COD)	0,99471
Adj. R-Square	0,99468

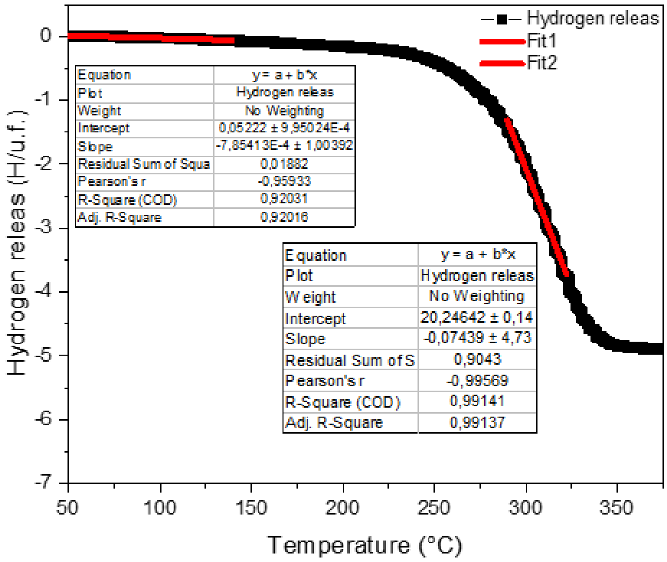
Temperature Programmed Desorption: Sample D hydrogen release

Equation	y= a + b*x
Plot	Hydrogen releas
Weight	No Weighting
Intercept	0,05222 ± 9,95024E-4
Slope	-7,85413E-4 ± 1,00392
Residual Sum of Squa	0,01882
Pearson's r	-0,95933
R-Square (COD)	0,92031
Adj. R-Square	0,92016

Equation	y = a + b*x
Plot	Hydrogen releas
Weight	No Weighting
Intercept	20,24642 ± 0,14
Slope	-0,07439 ± 4,73
Residual Sum of S	0,9043
Pearson's r	-0,99569
R-Square (COD)	0,99141
Adj. R-Square	0,99137

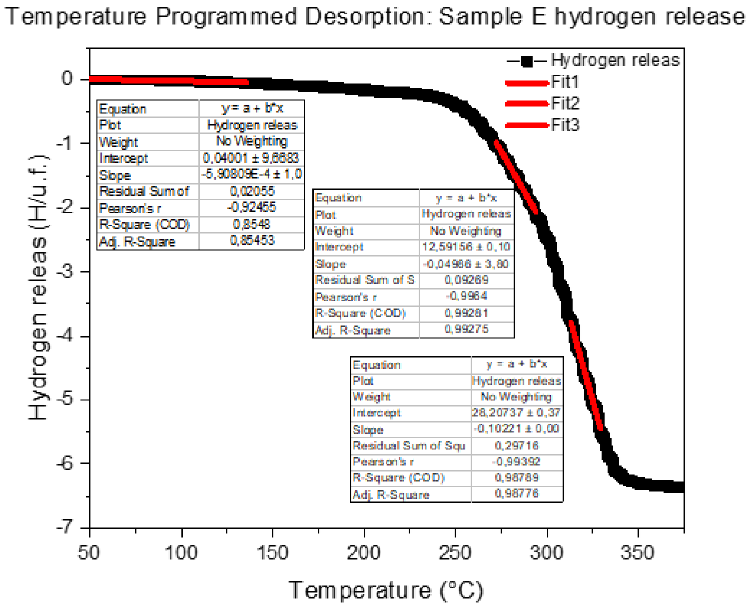

Equation	y= a + b*x
Plot	Hydrogen releas
Weight	No Weighting
Intercept	0,04001 ± 9,6683
Slope	-5,90809E-4 ± 1,0
Residual Sum of	0,02055
Pearson's r	-0,92455
R-Square (COD)	0,8548
Adj. R-Square	0,85453

Equation	y = a + b*x
Plot	Hydrogen releas
Weight	No Weighting
Intercept	12,59156 ± 0,10
Slope	-0,04986 ± 3,80
Residual Sum of S	0,09269
Pearson's r	-0,9964
R-Square (COD)	0,99281
Adj. R-Square	0,99275

Equation	y = a + b*x
Plot	Hydrogen releas
Weight	No Weighting
Intercept	28,20737 ± 0,37
Slope	-0,10221 ± 0,00
Residual Sum of Squ	0,29716
Pearson's r	-0,99392
R-Square (COD)	0,98789
Adj. R-Square	0,98776

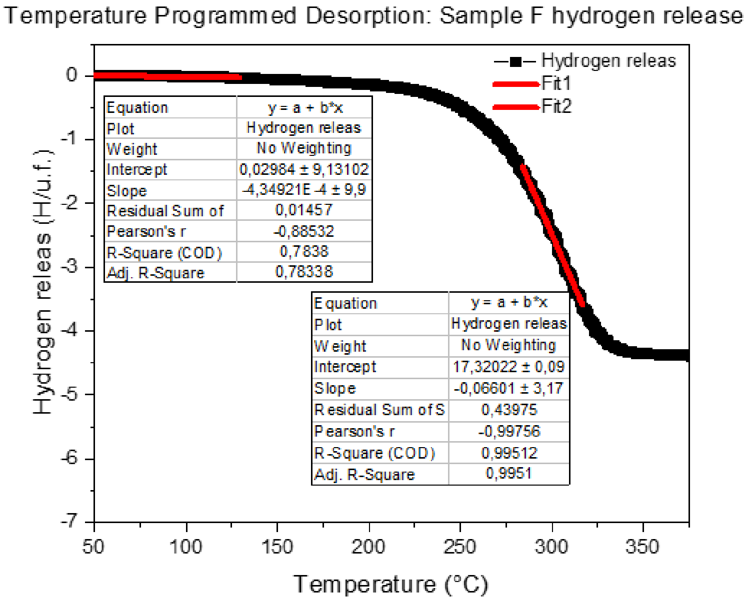

Equation	y = a + b*x
Plot	Hydrogen releas
Weight	No Weighting
Intercept	0,02984 ± 9,13102
Slope	-4,34921E-4 ± 9,9
Residual Sum of	0,01457
Pearson's r	-0,88532
R-Square (COD)	0,7838
Adj. R-Square	0,78338

Equation	y = a + b*x
Plot	Hydrogen releas
Weight	No Weighting
Intercept	17,32022 ± 0,09
Slope	-0,06601 ± 3,17
Residual Sum of S	0,43975
Pearson's r	-0,99756
R-Square (COD)	0,99512
Adj. R-Square	0,9951

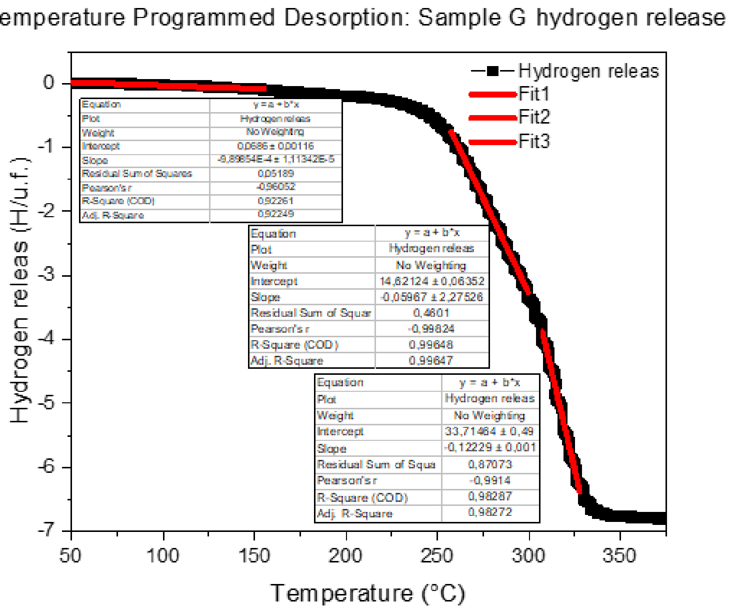

Figure 3.6: Analysis of the desorption temperature using the tangent method to find the onset temperature: a) Sample A, b) Sample B, c) Sample C, d) Sample D, e) Sample E, f) Sample F, g) Sample G

3.4 XRD after Desorption

Analyzing the XRD after desorption, it is possible to distinguish peaks that can be attributed to Fe and Mg type phases present in the majority of the X-ray diffraction patterns. For Fe, the first peak is at 52 degrees, followed by peaks at 77 degrees and 100 degrees. For Mg, it has peaks at 37, 40, 42, 56, 67, 74, 81, and 83 degrees.

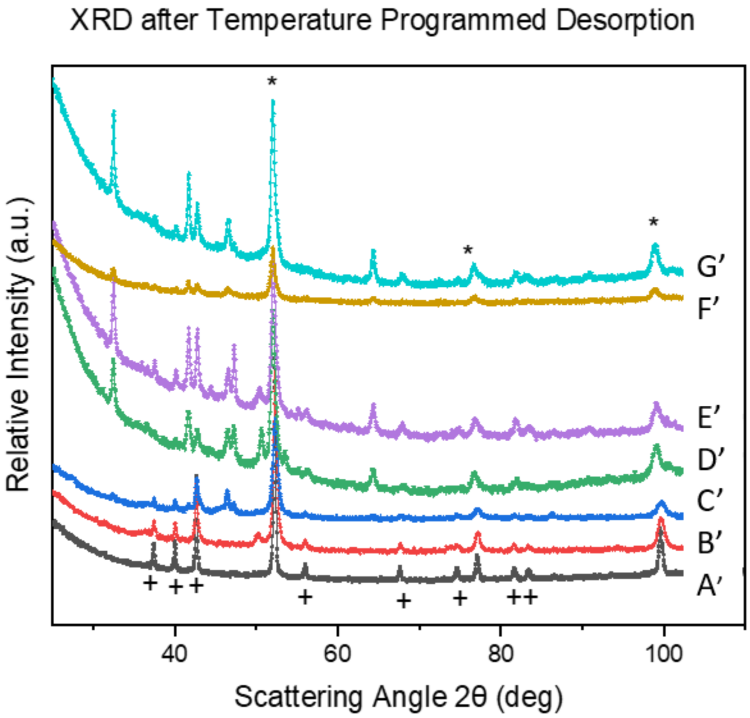

Figure 3.7: Comparison of all the XRD after temperature programmed desorption. Peaks belonging to the Fe phase are indicated with *, and peaks belonging to the Mg phase are indicated with +.

For the samples after desorption, all the phases present in each XRD pattern were identified and are presented in the following table.

Sample	Phases	Space group
A'	Mg	P63/mmc
	Fe	$Im\bar{3}m$
B'	Mg	P63/mmc
	Fe	$Im\bar{3}m$
	MgCo	$Im\bar{3}m$
C'	FeNi	$Im\bar{3}m$
	MgFeNi	$P6_222$
	Mg	P63/mmc
	MgCo	$Im\bar{3}m$
D'	MgCo	$Im\bar{3}m$
	Fe	$Im\bar{3}m$
	Mg	P63/mmc
	MnFe	$P4_132$
E'	Mg	P63/mmc
	MgNi	P63/mmc
	MnFe	$Im\bar{3}m$
	MgCo	$Im\bar{3}m$
F'	MgCo	$Im\bar{3}m$
	Mg	P63/mmc
	MnFe	$P4_132$
	CrFe	$Im\bar{3}m$
G'	CrFe	$Im\bar{3}m$
	Mg	P63/mmc
	MgCo	$Im\bar{3}m$
	MnFe	$P4_132$

Table 3.4: Phases and space groups for each sample after TPD

3.5 Absorption and desorption kinetics

Additional investigations were conducted on samples C and G to examine their kinetic properties. For sample C, a mass of 297.8mg was loaded, whereas for sample G, a mass of 300mg was loaded. The furnace was heated to 320 °C to carry out the measurements. The results obtained are shown in figures 3.8 and 3.9.

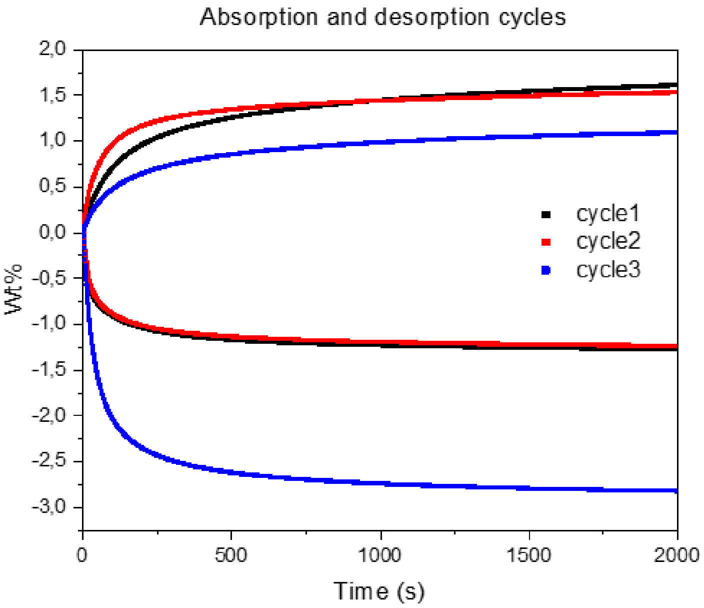

Figure 3.8: Sample C kinetics

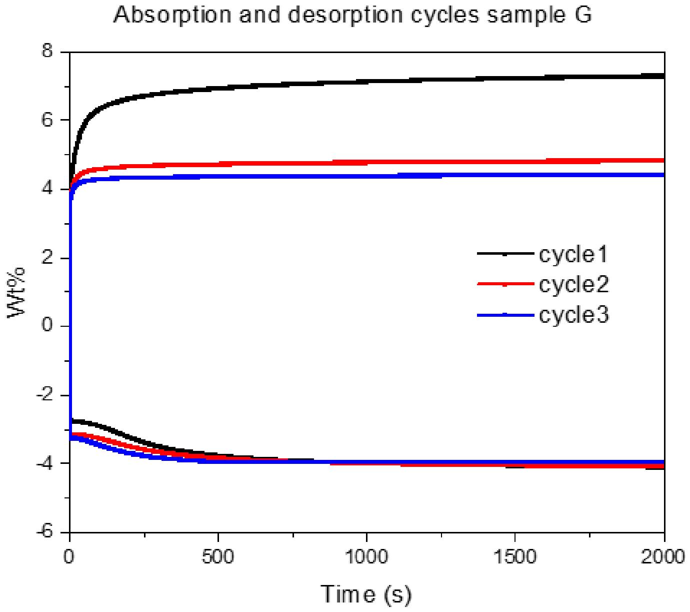

Figure 3.9: Sample G kinetics

Regarding both sample C and sample G, the hydrogen absorbed and desorbed is significantly lower than the values obtained after RBM and TPD. It is likely that both absorption and desorption processes were not completed, and by waiting for a sufficiently long time, more realistic values could have been obtained. For sample C, it can be observed that in the third cycle, the amount of desorbed hydrogen is significantly higher than in the previous two cycles. This occurred because during the absorption phase of the third cycle, after 2000 seconds, the absorption was forced and facilitated by doubling the pressure. As a result, even though it is not visible from the graph, a higher total absorption is achieved compared to the two previous cycles, justifying the subsequent desorption. For sample G, the cycles were initiated with absorption since the sample had previously been completely desorbed. As a result, we observe a higher absorption in the first cycle, but it reaches values that are not consistent with those previously obtained through RBM. Additionally, for sample G, it can be noted that desorption occurs in two steps, as previously observed during the TPD.

3.6 PCI

On samples C and G, measurements of PCI in absorption and desorption were also conducted, as observable in Figures 3.10 and 3.11. The temperature was 320°C. The equilibrium pressures found are displayed in Table 3.5. Subsequently, an average of the values obtained in the absorption and desorption PCI was calculated to estimate the actual plateau pressure value with greater accuracy.

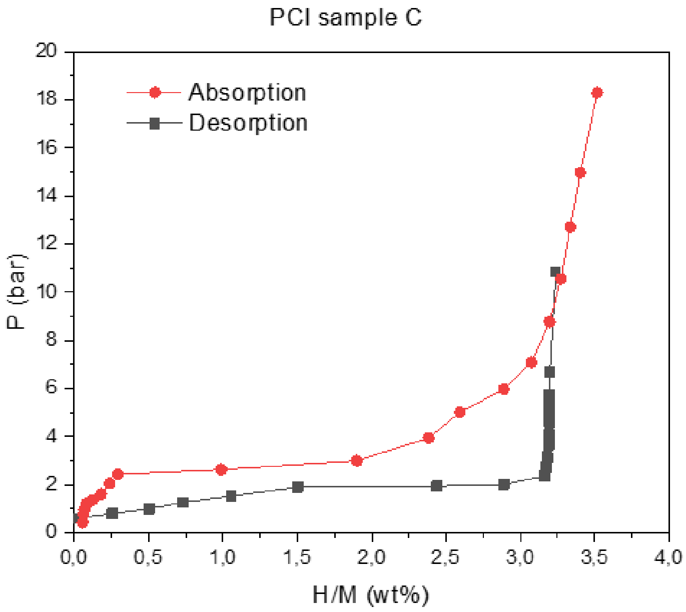

Figure 3.10: PCI sample C

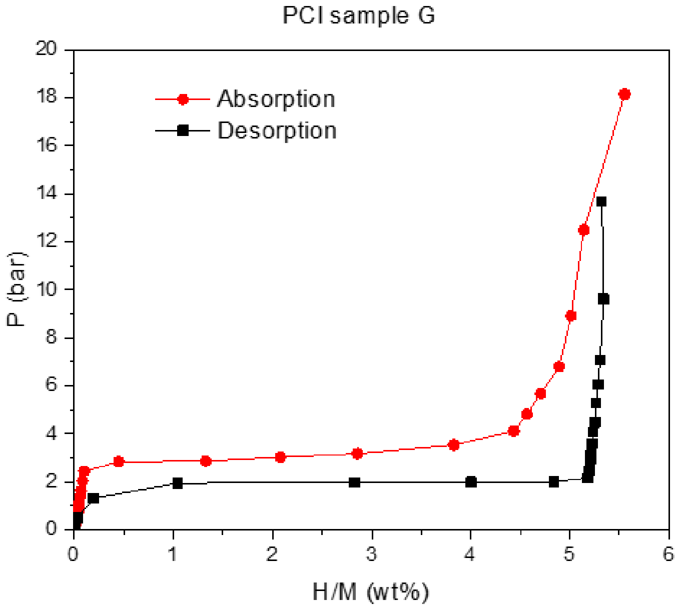

Figure 3.11: PCI sample G

Table 3.5: Plateau pressure values for samples C and G.

Sample	Plateau pressure abs. (bar)	Plateau pressure des. (bar)	Average plateau pressure (bar)
C	2.85	1.94	2.40
G	3.02	1.96	2.49

As for the amount of hydrogen absorbed, the values obtained are in good agreement with the results obtained during reactive ball milling and TPD (Temperature Programmed Desorption), although the samples absorbed a lower amount of hydrogen than expected. This could be due to the fact that in reactive ball milling, the process involves powder mechanics where solid particles are mixed and finely ground. This process can increase the surface area of the sample and facilitate chemical reactions between the sample and hydrogen.

In the Pressure Composition Isotherm (PCI) absorption process, the sample is exposed to hydrogen under high pressure and controlled temperature. This process may be less effective in introducing hydrogen into the sample if the conditions are not optimal for the reaction. Additionally, the duration of the treatment in reactive ball milling, which in our case was approximately 20 hours, can influence the amount of hydrogen absorbed compared to a 10-hour PCI. In fact, a longer treatment period could lead to greater absorption.

3.7 XRD after PCI

By examining the X-ray diffraction (XRD) patterns following absorption PCIs of sample C and G, it becomes feasible to identify distinct peaks that can be associated with MgH_2, Fe phases, and a complex hydride phase. These qualitative results are consistent with those obtained with the XRD after reactive ball milling (Table 3.2), confirming the production of complex hydrides after sample absorptions. The XRD measurements were taken from 20 to 105 degrees and the radiation used is of the Cu K-alpha type with a typical wavelength of 1.54 Ångströms.

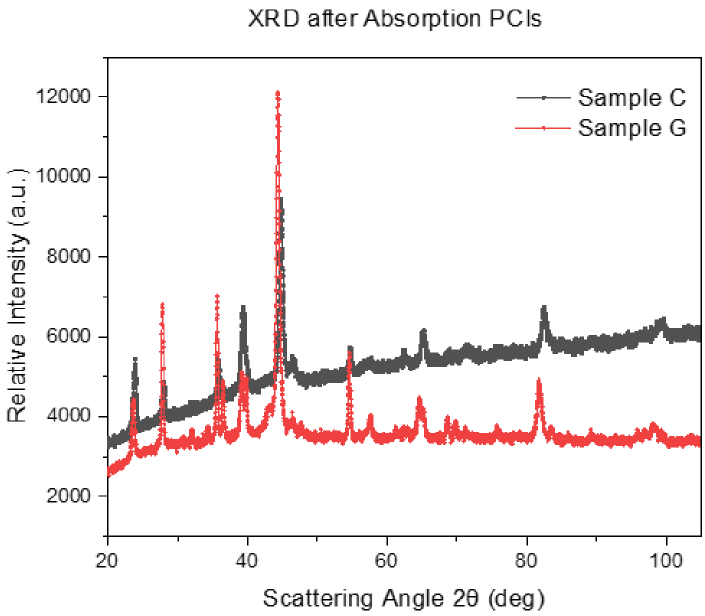

Figure 3.12: XRD patterns of samples C and G after absorption PCIs

Chapter 4

Conclusions

It was validated the synthesis and characterization methods. The materials studied so far (Mg_2FeH_6, $Mg_2Fe_{0.5}Co_{0.5}H_{5.5}$) have similar capacities and thermodynamics as those reported in the literature. The study of another new targeted compound ($Mg_2Fe_{0.3}Co_{0.3}Ni_{0.3}H_x$, $Mg_2Fe_{0.25}Co_{0.25}Ni_{0.25}Mn_{0.25}H_x$, $Mg_3Fe_{0.25}Co_{0.25}Ni_{0.25}Mn_{0.25}H_x$, $Mg_2Fe_{0.2}Co_{0.2}Ni_{0.2}Mn_{0.2}Cr_{0.2}H_x$, $Mg_3Fe_{0.2}Co_{0.2}Ni_{0.2}Mn_{0.2}Cr_{0.2}H_x$) was done starting from the synthesis, and then the hydrogenation reversibility was studied, obtaining that the majority of hydrogen absorbed during the synthesis can be desorbed. Moreover, it was observed that the amount of Mg, whether using $y = 2$ or 3, influenced the nature of phases formed during the synthesis. In fact, single-phase hydrides were obtained for samples A, B, C, D, F where $y = 2$, and two-phase hydrides were obtained for samples E and G where $y = 3$. Intermetallic phases were obtained for all the samples. In particular, during reactive ball milling (RBM), it was observed that the hydrogen absorption and release should ideally be equal for perfect reversibility of the reaction. However, some samples showed discrepancies: in some cases, the hydrogen release was lower than the absorption, suggesting partial reversibility, while in other cases, the release exceeded absorption, but measurement errors made the values acceptable. In one sample, there may have been an underestimation of the measurement error. Furthermore, from X-ray diffraction (XRD) after RBM, it was found that all the expected hydride compounds were formed with varying weight fractions except for one sample. It was noted that samples with more Mg atoms formed lower amounts of hydride compared to samples with fewer Mg atoms, but both produced MgH_2. Lastly, the results from Temperature Programmed Desorption (TPD) showed that the onset temperatures did not vary significantly with the addition of transition metals, indicating similarity in desorption kinetics and thermal stability among the samples.

For the samples C and G it was performed a study of the kinetics of the different materials and Pressure-Composition Isotherm (PCI) curves to find the plateau pressures.

Bibliography

[1] Yartys, Lototskyy, Akiba, Albert, Antonov, Ares, Baricco, Bourgeois, Buckley, Bellosta von Colbe, Crivello, Cuevas, Denys, Dornheim, Felderhoff, Grant, Hauback, Humphries, Jacob, Jensen, de Jongh, Joubert, Kuzovnikov, Latroche, Paskevicius, Pasquini, Popilevsky, Skripnyuk, Rabkin, Sofianos, Stuart, Walker, Hui Wang, Webb, Min Zhu, ”Magnesium based materials for hydrogen based energy storage: Past, present and future”, international journal o f hydrogen energy, 44 (2019), 7809 -7859

[2] Pasquini, Sakaki, Akiba, D Allendorf, Alvares, Ares, Babai, Baricco, von Colbe, Bereznitsky, Buckley, Whan Cho, Cuevas, de Rango, Dematteis, Denys, Dornheim, Fernández, Hariyadi, Hauback, Wook Heo, Hirscher, Humphries, Huot, Jacob, Jensen, Jerabek, Young Kang, Keilbart, Kim, Latroche, Leardini, Li, Ling, Lototskyy, Mullen, Orimo, Paskevicius, Pistidda, Polanski, Puszkiel5, Rabkin, Sahlberg, Sartori, Santhosh, Sato, Shneck, Sørby, hang, Stavila, Suh, Suwarno, Thu, Wan, Webb, Witman, Wan, Wood, Yartys, TOPICAL REVIEW: ”Magnesium- and intermetallic alloys-based hydrides for energy storage: modelling, synthesis and properties”, Prog. Energy, 4 (2022), https://doi.org/10.1088/2516-1083/ac7190

[3] L. Schlapbach, A. Zuttel Hydrogen-storage materials for mobile applications, Nature 414, p. 353-358, (2001)

[4] M. Chiaretta, Sistemi di distribuzione e stoccaggio di idrogeno, Tesi di Laurea, Politecnico di Torino (2003).

[5] Ley, M.B.; Jepsen, L.H.; Lee, Y.-S.; Cho, Y.W.; Bellosta von Colbe, J.M.; Dornheim, M.; Rokni, M.; Jensen, J.O.;Sloth, M.; Filinchuk, Y.; et al. Complex hydrides for hydrogen storage—New perspectives. Mater. Today 2014,17, 122–128

[6] Jepsen, L.H.; Ley, M.B.; Lee, Y.-S.; Cho, Y.W.; Dornheim, M.; Jensen, J.O.; Filinchuk, Y.; Jørgensen, J.E.;Besenbacher, F.; Jensen, T.R. Boron–nitrogen based hydrides and reactive composites for hydrogen storage.Mater. Today 2014, 17, 129–135.

[7] Bogdanovi c, B.; Schwickardi, M. Ti-doped alkali metal aluminium hydrides as potential novel reversiblehydrogen storage materials. J. Alloys Compd. 1997, 253–254, 1–9.

[8] Züttel, A.; Wenger, P.; Rentsch, S.; Sudan, P.; Mauron, P.; Emmenegger, C. LiBH4 a new hydrogen storagematerial. J. Power Sources 2003, 118, 1–7.

[9] T.N. Dymova, Z.K. Sterlyadkina, V.G. Safronov On the preparation of magnesium hydride Russ J Inorg Chem, 6 (1961), pp. 763-767

[10] J. Zhang, F. Cuevas, W. Zaïdi, J.-P. Bonnet, L. Aymard, J.-L. Bobet, M. Latroche, "Highlighting of a single reaction path during reactive ball milling of Mg and TM by quantitative H2 gas sorption analysis to form ternary complex hydrides (TM = Fe, Co, Ni)", J. Phys. Chem. C, 115 (2011) 4971-4979, doi: http://dx.doi.org/10.1021/jp2005293.

[11] Borislav Bogdanovic´, Alexander Reiser, Klaus Schlichte, Bernd Spliethoff, Bernd Tesche. Thermodynamics and dynamics of the Mg–Fe–H system and its potential for thermochemical thermal energy storage. J. Alloys Comp., 345 (2002), 77–89

[12] S. Deledda and B. C. Hauback. The formation mechanism and structural characterization of the mixed transition-metal complex hydride Mg2(FeH6)0.5(CoH5)0.5 obtained by reactive milling. Journal of Nanotechnology, 20 (2009), 204010.

[13] R. Martínez-Coronado, M. Retuerto, J.A. Alonso, "Simplified mechano-synthesis procedure of Mg2NiH4", International Journal of Hydrogen Energy Volume 37, Issue 5, March 2012, Pages 4188-4193

[14] Kristina Spektor, Wilson A. Crichton, Stanislav Filippov, Sergei I. Simak and Ulrich Haussermann, "Exploring the MgCrH System at High Pressure and Temperature via in Situ Synchrotron Diffraction", Inorg. Chem. 2019, 58, 1104311050

[15] Kristina Spektor, Wilson A. Crichton, Sumit Konar, Stanislav Filippov Johan Klarbring, Sergei I. Simak and Ulrich Haussermann, "Unraveling Hidden MgMnH Phase Relations at High Pressures and Temperatures by in Situ Synchrotron Diffraction", Inorg. Chem. 2018, 57, 16141622

[16] Y. Verbovytskyy, J. Zhang, F. Cuevas, V. Paul-Boncour, I. Zavaliy, "Synthesis and properties of the Mg2Ni0.5Co0.5H4.4 hydride", J. Alloys Comp., 645 (2015) S408-S411

[17] Møller, K. T., Sheppard, D., Ravnsbæk, D. B., Buckley, C. E., Akiba, E., Li, H. W., Jensen, T. R. (2017). Complex metal hydrides for hydrogen, thermal and electrochemical energy storage. Energies, 10(10), Article 1645. https://doi.org/10.3390/en10101645

[18] H Hemmes, A Driessen and R Griessen, ”Thermodynamic properties of hydrogen at pressures up to 1 Mbar and temperatures between 100 and 1000 K”, J. Phys. C: Solid State Phys. 19 (1986) 3571-3585. Printed in Great Britain

[19] Felipe Marques, a Mateusz Balcerzak, ab Frederik Winkelmann, a Guilherme Zepon cd and Michael Felderhoff, ”Review and outlook on high-entropy alloys for hydrogen storage”, Energy Environ. Sci., 2021, 14, 5191